Coulomb Interaction-Driven Entanglement of Electrons on Helium

Niyaz R. Beysengulov
Department of Physics and Astronomy, Michigan State University, East Lansing, Michigan 48824, USA

Øyvind S. Schøyen, Stian D. Bilek, Jonas B. Flaten, and Oskar Leinonen
Department of Physics and Center for Computing in Science Education, University of Oslo, Oslo N-0316, Norway

Morten Hjorth-Jensen[*]
Facility for Rare Isotope Beams and Department of Physics and Astronomy, Michigan State University, East Lansing, Michigan 48824, USA
and Department of Physics and Center for Computing in Science Education, University of Oslo, Oslo N-0316, Norway

Johannes Pollanen
Department of Physics and Astronomy, Michigan State University, East Lansing, Michigan 48824, USA

Håkon Emil Kristiansen
Department of Chemistry and Hylleraas Center for Quantum Molecular Sciences, University of Oslo, Oslo N-0316, Norway

Zachary J. Stewart, Jared D. Weidman, and Angela K. Wilson
Department of Chemistry, Michigan State University, East Lansing, Michigan 48824, USA

(Received 25 January 2024; revised 29 April 2024; accepted 12 July 2024; published 6 August 2024)

The generation and evolution of entanglement in many-body systems is an active area of research that spans multiple fields, from quantum information science to the simulation of quantum many-body systems encountered in condensed matter, subatomic physics, and quantum chemistry. Motivated by recent experiments exploring quantum information processing systems with electrons trapped above the surface of cryogenic noble gas substrates, we theoretically investigate the generation of *motional* entanglement between two electrons via their unscreened Coulomb interaction. The model system consists of two electrons confined in separate electrostatic traps that establish microwave-frequency quantized states of their motion. We compute the motional energy spectra of the electrons, as well as their entanglement, by diagonalizing the model Hamiltonian with respect to a single-particle Hartree product basis. We also compare our results with the predictions of an effective Hamiltonian. The computational procedure outlined here can be employed for device design and guidance of experimental implementations. In particular, the theoretical tools developed here can be used for fine-tuning and optimization of control parameters in future experiments with electrons trapped above the surface of superfluid helium or solid neon.

DOI: 10.1103/PRXQuantum.5.030324

I. INTRODUCTION

Entanglement is the fundamental characteristic that distinguishes interacting quantum many-body systems from their classical counterparts. The study of entanglement in precisely engineered quantum systems with countably many degrees of freedom is at the forefront of modern physics, and it is a key resource in quantum information science. This is particularly true in the development of two-qubit logic for quantum computations, which has been demonstrated in a wide variety of physical systems used in present-day quantum computing, including superconducting circuits [1,2], trapped ions [3,4], semiconductor quantum dots [5–8], color-center defects in diamond [9–11], and neutral atoms in optical lattices [12,13]. Investigating the generation and evolution of entanglement in quantum many-body systems is also important for quantum simulations [14–17], having the potential to advance the fundamental understanding of dense nuclear matter

---

[*] Contact author: morten.hjorth-jensen@fys.uio.no

or high-energy physics [18–22], correlated electron systems [23–25], and quantum chemistry [26–28]. Quantum simulators based on *natural* qubits such as atoms [29–31], ions [32,33], and photons [34] are particularly appealing since these systems are highly programmable, controllable, and replicable [35]. Additionally, in these systems the coupling to decohering environmental degrees of freedom is minimal, allowing for a tight feedback between experiments and theory.

Trapped electron systems represent a novel approach to investigating the generation of entanglement, sharing many features with platforms based on other natural qubit systems. Recent experimental efforts have investigated the feasibility of trapped electron qubits using ion trap techniques [36,37]. In fact, the naturally quantized motion of electrons trapped in vacuum above the surface of superfluid helium was one of the earliest theoretical proposals for building a large-scale analog quantum computer [38]. The surface of the superfluid functions as a pristine substrate [39], shielding the electrons from deleterious sources of noise at the device layer beneath helium. Since this initial proposal, a number of theoretical ideas have been put forward to create both charge [40–44] and spin [42,44–46] qubits based on these trapped electrons. Additionally, a wide variety of experimental work, directed at realizing these electronic qubits, has been performed to leverage advances in nanofabrication techniques for precision trapping and control of electrons on helium in confined geometries [47–51], mesoscopic devices [52–54], circuit quantum electrodynamic architectures [55,56], and surface-acoustic-wave devices [57]. Single-electron trapping and detection have been experimentally achieved [52,56,58], as well as extremely high-fidelity electron transfer along gated arrays fabricated using standard CMOS processes [59]. Similarly, electrons trapped above the surface of solidified noble gases offer an alternative trapped electron qubit; electrons trapped in vacuum above the surface of solid neon have recently been experimentally demonstrated as a novel natural charge qubit [60] with high coherence [61].

In aggregate, these technological advances have opened the door to exploring the generation and evolution of entanglement in systems based on trapped electrons. Here we present a model system for investigating the entanglement between the microwave-frequency motional states of two electrons trapped in vacuum above the surface of a layer of superfluid helium. The electrons are confined laterally by applying voltages to electrodes in a substrate beneath the condensed helium layer. These voltages are tuned to set up electrostatic traps on the helium surface to control the relative position of the electrons and quantize their in-plane motional states in the gigahertz-frequency range. We utilize the full configuration-interaction (CI for short in this work) method [62] for distinguishable particles to compute the quantized motional excitations of the system, as well as the entanglement between the electrons generated by Coulomb interaction. These numerical studies are in turn used to optimize the electrode voltages to maximize the entanglement. We also present an effective theoretical model of the two-electron system, as a useful tool to analyze the underlying coupling mechanism between the electrons. Given the exact solution provided by the CI calculations, we discuss the limitations of the approximations of this effective model. Our work can be used to provide feedback to future experimental realizations in which, ultimately, control and readout of charged qubit states can be achieved, via integration of microwave resonators [42,56,60,61] using standard techniques based on circuit quantum electrodynamics (cQED) [63].

The system of two electrons electrostatically confined above the helium surface conceptually shares some similarities with double quantum dots created in semiconductors [64]. The correlated behavior of electrons in these double quantum dots have been studied theoretically [8, 65–70], as well as experimentally in gallium arsenide [6,71,72] and silicon germanium [73] heterostructures. Unlike these semiconductor systems, electrons on helium are quantum nondegenerate [74] and do not experience the decohering environment inherent to these more conventional quantum dot systems. Similarly, the lack of complicated many-body effects from the environment (i.e., the impact of band structure, excitonic degrees of freedom, etc.) makes electrons on helium a unique platform for comparing theory with experiments for charge qubits.

In Sec. II we present a schematic microdevice that allows for controlled Coulomb-driven entanglement between two electrons. We also describe a numerical procedure to find the optimal parameters for this device to function as a two-qubit quantum computer. Section III contains our main results, with detailed discussion of the system properties and comparison to an effective model Hamiltonian. The final section contains conclusions, perspectives, and an outlook for future work. Additional details are presented in various appendices.

II. DEVICE AND THEORY

Electrons placed in vacuum above a layer of liquid helium are drawn toward the liquid by an attractive force produced by positive image charges in the dielectric liquid. However, the electrons are prevented from entering the liquid by a large (about 1 eV) Pauli barrier at the liquid-vacuum interface [75,76]. The balancing of these two effects creates a ladder of Rydberg-like states for the vertical motion of the electrons, and at low temperatures the electrons are naturally initialized into the ground state of this motion approximately 11 nm above the helium surface [77,78]. The electrons experience only a weak interaction with their environment, which is mainly governed by interactions with thermally excited ripplons (quantized capillary waves on the helium surface) and phonons in the bulk of the liquid [79]. Based on these interactions, theory predicts long coherence times of both the electron spin and motional degrees of freedom [40,45,46]. The electron in-plane motion can be further localized on length scales approaching an electron separation of around 1 µm through the integration of microdevices that provide lateral confinement [50,53,56]. Devices of this type have been used to demonstrate single-electron trapping [52,56,60], and to investigate the two-dimensional crystalline electronic phase known as the Wigner solid [50,80], which arises from the largely unscreened Coulomb repulsion between the electrons. As explored in this work, this strong electron-electron interaction can also in principle be utilized to couple the quantum motion of electrons and create entanglement between electron charge qubits, in analogy to a Cirac-Zoller entangling gate [81].

A. Device design

A schematic microdevice for investigating the Coulomb-driven entanglement of the in-plane motional states of two electrons on helium is sketched in Fig. 1(a). Here we consider a (3 × 1)-µm^2 size microchannel structure with a depth of 0.5 µm, filled with superfluid helium via capillary action [47]. Once the device is filled, thermionic emission from a tungsten filament located above the helium surface can be used to generate electrons, which are then naturally trapped above the liquid surface. We note that trapping one or two electrons also requires controlled loading and unloading of electrons into the trap region from a larger reservoir area where electrons are stored [not shown in Fig. 1(a)]. This type of electron manipulation is quite standard and has been experimentally demonstrated in multiple devices; see, for example, Refs. [56,59]. For the purpose of the current theoretical study, we consider a simple array of electrodes that allow for the investigation of entanglement between two electrons, which we assume have already been loaded successfully into the device. The rectangular device geometry and dimensions were chosen to create an in-plane motional quantization axis along the x direction, with energy gaps in the frequency range of 5–15 GHz. These states are decoupled from motional states along the y direction at significantly higher, approximately 6 times larger, frequency. Because of this large separation in frequency, we ignore the states directed along the y axis in this one-dimensional study. Voltages applied to seven 200-nm-wide electrodes spaced by 200 nm beneath the helium layer provide the degrees of freedom needed to form an electrostatic double-well potential for the two electrons, as shown in Figs. 1(b) and 1(c). The electrostatic potential in the trap region is given by

$$\varphi(x,y) = \sum_{i=1}^{7} \alpha_i(x,y) V_i, \tag{1}$$

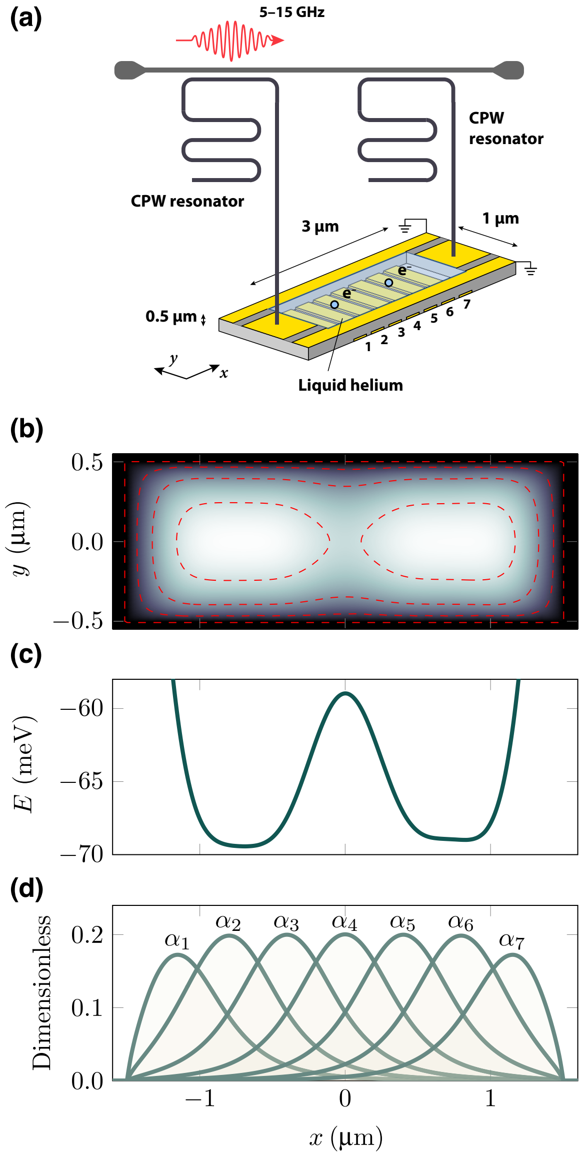

FIG. 1. (a) Schematic microdevice, in which two electrons are trapped on the surface of a liquid helium basin in a double-well potential created by electrodes 1–7. Control and readout of the quantized motion is provided by two superconducting coplanar waveguide resonators, dispersively coupled to the in-plane motional states of the electrons. (b) Example configuration for the full two-dimensional electrostatic potential at the helium surface $z = 0.5$ µm in the device, which realizes two separate wells. Brighter colors represent a stronger potential given in arbitrary units. (c) One-dimensional linecut of the potential in (b) along $y = 0$. (d) One-dimensional coupling constants from each individual electrode beneath the helium layer along $y = 0$ and $z = 0.5$ µm. These coupling constants give rise to the total potential as given by Eq. (1).

where $\alpha_i = C_i/C_\Sigma$ is the relative contribution to the potential defined by the capacitance between a region of space at position (x, y) on the helium surface and the corresponding electrode. The total capacitance is $C_\Sigma = \sum_i C_i$, and V_i

is the voltage applied to the ith electrode, which can be adjusted to create particular trapping potential configurations. We note that the top electrodes at the helium surface are held at ground potential. The coupling constants $\alpha_i(x, y)$ are calculated by solving the Laplace equation for the electrostatic potential numerically, using standard finite-element modeling techniques [see Fig. 1(d)]. The double-well trap is achieved by applying a negative voltage to the central electrode [electrode 4 in Fig. 1(a)] and positive voltages to the other electrodes. Particular choices of applied voltages will be described further in Sec. III, where we also discuss how this setup allows us to adjust the electron motional frequencies over a broad range, thereby enabling the generation of entanglement between the two electrons at certain conditions. We note that thicker layers of helium lead to stronger screening of the bottom electrodes by the top ones, reducing the coupling constants from the seven control electrodes. By choosing a specific helium thickness of $z = 0.5\,\mu\text{m}$ we aim at ensuring sufficiently high anharmonicities (greater than 500 MHz) of the traps as thicker layers induce more harmonic trapping potentials.

Coherent control and readout of the electron motional states in this type of microdevice is based on coupling the electron motional states to microwave frequency photons in superconducting coplanar waveguide resonators [see Fig. 1(a)], with a coupling $g_{\text{RF}}/2\pi = \langle 1|\mathbf{d}\cdot\mathbf{E}|0\rangle = ef_{\text{RF}}\partial\alpha_{\text{RF}}/\partial x\sqrt{Z_{\text{RF}}/m_e\omega_{\text{e}}}$ [56]. In this expression $\mathbf{d}$ is the dipole moment of the oscillating electron along the x axis, $\mathbf{E} = \partial\alpha_{\text{RF}}/\partial x\cdot V_{\text{zpf}}\hat{\mathbf{x}}$ is the electric field created by the resonator at the position of the electron, e and m_e are the electron charge and mass, respectively, α_{RF} is the coupling constant for the resonator electrode, V_{zpf} is the voltage amplitude of zero-point fluctuations in the resonator, f_{RF} and Z_{RF} are resonator frequency and impedance, and ω_{e} is the electron motional frequency along the x axis. For typical values of $\partial\alpha_{\text{RF}}/\partial x = 0.5\times10^6\ \text{m}^{-1}$, $Z_{\text{RF}} = 50\ \Omega$, $f_{\text{RF}} = 7$ GHz, and $\omega_{\text{e}}/2\pi = 5$ GHz, we find that $g_{\text{RF}}/2\pi \simeq 12$ MHz.

At low temperatures, the decay of energy from the electrons-on-helium system occurs due to its interaction with helium surface ripplons and bulk phonons (see, for example, Refs. [40,46]). The total rate of decoherence due to these processes has been estimated to be approximately $\Gamma/2\pi = 3\times10^4$ Hz [40], allowing the realization of the strong coupling regime ($g_{\text{RF}} \gg \Gamma$) between the microwave photons and the electron motional states.

In this device, the two electrons are coupled individually to two superconducting coplanar waveguide (CPW) $\lambda/4$ resonators, each having a different resonant frequency. The crosstalk coupling between an electron and the other electron's resonator is approximately 40 times smaller than the direct coupling to its own resonator, so we ignore this in our analysis. It should be noted that this classical crosstalk can ultimately limit the fidelity of gate operations, but it can be mitigated by applying appropriate compensation tones [82]. In the dispersive regime of cQED, in which $g_{\text{RF}}/|\omega_{\text{e}} - \omega_{\text{RF}}| \ll 1$, the frequency of the resonator is sensitive to the state of the electronic motion, which can be detected by measuring the transmitted microwave signals through the CPW feedline connected to the resonators [42,56,63].

B. Model Hamiltonian

Our model Hamiltonian describes two electrons trapped in a double-well potential set up by seven electrodes as given in Eq. (1), but we restrict our calculations along the x direction only. The interaction between the electrons is given by a Coulomb term that gives rise to their correlated motion. The full Hamiltonian for the system, in dimensionless units, is then given by

$$\hat{H} = \sum_{i=1}^{2}\left(-\frac{1}{2}\frac{\mathrm{d}^2}{\mathrm{d}x_i^2} + v(x_i)\right) + u(x_1, x_2), \tag{2}$$

where $v(x) = -e\varphi(x)/E_d$ is the trap potential. Here, $\varphi(x) = \varphi(x, 0)$ is the electrostatic trap potential given in Eq. (1), and $E_{\text{d}} = \hbar^2/m_{\text{e}}x_0^2$ is our energy unit ($\hbar$ is the reduced Planck constant). The value $x_0 = 123$ nm is our length unit, representing the characteristic interelectron distance corresponding to a typical electron density of $\simeq 2\times10^9\ \text{cm}^{-2}$ in microdevices [50]. The soft Coulomb interaction is given by

$$u(x_1, x_2) = \frac{\kappa}{\sqrt{(x_1 - x_2)^2 + \epsilon^2}}, \tag{3}$$

where $\kappa = e^2/(4\pi\varepsilon_0 E_{\text{d}}) = 2326$ gives the strength of the Coulomb interaction (ε_0 is the vacuum permittivity). We have introduced a shielding parameter $\epsilon = 10^{-2}$ to remove the singularity at $x_1 = x_2$ [83]. We note that, due to the small distance between the electrons and the underlying electrodes, the Coulomb interaction will be reduced due to screening effects. However, in our analysis we consider an unscreened Coulomb interaction, which sets an upper bound for the interaction strength between the two electrons. We also omit coupling of the electrons to the ripplons in our study (see details in Appendix A).

Here we consider deep potentials $v(x)$ with barrier height $\simeq 80$ meV and separated at the distance $\simeq 1.7\,\mu\text{m}$, which prohibits tunneling through the barrier between the wells for the bound electron states.

This encourages us to split the potential into two separate wells. Denoting the position of the barrier maximum by x_b, we can define

$$v^L(x) = \begin{cases} v(x), & x < x_b, \\ v(x_b), & x \geq x_b, \end{cases} \tag{4a}$$

$$v^R(x) = \begin{cases} v(x_b), & x < x_b, \\ v(x), & x \geq x_b, \end{cases} \tag{4b}$$

with L and R labeling the left and right wells, respectively. We can then express the total double-well potential as the sum $v(x) = v^L(x) + v^R(x) - v(x_b)$. Since there is negligible spatial overlap between single-electron states in different wells, we can omit spin and focus on motional product states in which one electron is localized in the left well while the other electron is localized in the right well.

In essence, a sufficiently deep double-well trap allows us to treat the electrons as distinguishable particles, labeled by their position [84]. The one-body Hamiltonian for each electron can then be written as

$$\hat{h}^A = -\frac{1}{2}\frac{\mathrm{d}^2}{\mathrm{d}x^2} + v^A(x) \tag{5}$$

with $A \in \{L, R\}$, and the two-body Hamiltonian is given by Eq. (2).

Throughout our analysis we vary the seven electrode voltages V_i to adjust the shape of the double-well potential $v(x)$, and hence also the energy spectrum and frequencies of our system. We refer to each such choice as a *well configuration*, and the tuning between configurations is what allows us to realize various quantum gates.

C. State ansatz

We solve the two-body problem described in the previous section by exact diagonalization of the Hamiltonian in Eq. (2) with respect to a single-particle product basis. The two-body state ansatz we use is

$$|\Phi_n\rangle = \sum_{i=0}^{N^L}\sum_{j=0}^{N^R} C_{ij,n}\left|\phi_i^L\phi_j^R\right\rangle. \tag{6}$$

Here, n is the index of each two-body energy eigenstate, and $\left|\phi_i^L\phi_j^R\right\rangle = \left|\phi_i^L\right\rangle \otimes \left|\phi_j^R\right\rangle$ are two-body product states built from two single-particle basis sets $\{|\phi_i^A\rangle \mid i = 0, \ldots, N^A\}$ (with $A \in \{L, R\}$). The above ansatz is analogous to the ansatz of full CI theory, but since our electrons are effectively distinguishable, we use separable product states instead of antisymmetrized Slater determinants in our expansion [62].

The quality of ansatz (6) depends on the choice of single-particle basis states $|\phi_i^A\rangle$. Even though we consider only two particles, a large single-particle basis will quickly make the exact diagonalization procedure prohibitively time consuming. This limits us to consider small single-electron basis sets, whose product states span the state space of our two-electron system to a good approximation. One option is to consider the eigenstates of the individual one-body Hamiltonians $\hat{h}^A$ defined in Eq. (5). However, this approach neglects all information about interactions and, as a consequence, still demands a significant number of basis states to accurately capture the physics. A more effective approach is to employ the Hartree method (analogous to the Hartree-Fock method, but for distinguishable particles), which incorporates the one-body Hamiltonian with a mean-field contribution from the Coulomb interaction. This method has the advantage of producing single-particle basis sets that can be truncated to only a few states while still capturing the interaction physics of the entangled two-body states within our system.

The construction of the Hartree basis sets $|\phi_i^A\rangle$ and derivation of the Hartree method are presented in Appendices B and C. With the single-particle basis sets established, the coefficients $C_{ij,n}$ in Eq. (6) can be calculated to find the full two-body energy eigenstates for each well configuration. This is done through a diagonalization procedure, which is explained in detail in Appendix D.

We should add, as discussed in more detail in Appendices B and D, that we also have performed full configuration-interaction calculations with an antisymmetrized wave-function basis for the two-electron system. For the system we are investigating, the Hartree ansatz with distinguishable particles gives an excellent approximation to the antisymmetrized full configuration-interaction calculations.

D. Entanglement

It is natural to consider the system at hand as bipartite, composed of the two electrons as, ideally, individual subsystems. Such a bipartition comes with the notion of entanglement—the inability to discern the exact state of each subsystem, even though the state of the full system is known. We aim to find certain well configurations for which a subset of the energy eigenstates are entangled, in order to enable the set up of two-qubit gates; see, for example, the discussions in Refs. [8,85,86].

A common entanglement measure for bipartite systems is the von Neumann entropy of a quantum state, defined as

$$S = -\mathrm{tr}[\hat{\rho}\log_2(\hat{\rho})], \tag{7}$$

where $\hat{\rho}$ is the reduced density operator of either subsystem. We use this measure to quantify entanglement and refer to it simply as the entropy. (See Appendix E for calculational details.) In what follows we denote the entanglement entropy of each energy eigenstate $|\Phi_n\rangle$ by S_n.

The two-body state of the full system can be expanded in any product state basis from the subsystems, such as in Eq. (6). While the Hartree basis discussed above provides a succinct picture of the *interaction* between subsystems, another basis offering a clear picture of the *entanglement* is the Schmidt basis, found by doing a singular-value decomposition of the coefficient matrix $C_{ij,n}$, as outlined in Appendix E. In the Schmidt decomposition of a two-body state, each term involves a product of unique, orthogonal Schmidt states. It follows that the Schmidt states are eigenstates of the reduced density operators of each subsystem. Then, the mixed state of each subsystem can be interpreted as a statistical ensemble of its Schmidt states, and the Schmidt coefficients (the singular values), when squared, give the occupation number of each Schmidt state. Our calculations indicate that the Hartree basis actually serves as an approximate common Schmidt basis for all the two-body energy eigenstates of our system. In addition to the von Neumann entropies S_n, we therefore map the two-body coefficients $C_{ij,n}$ to provide a clear overview of which products of single-electron states are involved in each entangled two-body state. For simplicity, we denote the Hartree product states as

$$|\phi_i^L \phi_j^R\rangle = |ij\rangle\,, \tag{8}$$

but note that these product states are not to be directly interpreted as computational basis states for quantum computing. We cannot do any measurements to collapse the two-electron system into any of these separable states, so they should be interpreted only as an ideal single-particle product basis for describing the two-body states of our system. The states that *should* be interpreted as computational basis states are four specific energy eigenstates of configuration I, as defined in Sec. II E below.

E. Gate operation

We target three specific well configurations that are ideal for operation of one-qubit rotations as well as two-qubit $\sqrt{i\text{SWAP}}$ and controlled-Z (CZ) gates [85,87,88]. Each configuration is defined through specific entanglement entropies of the two-body energy eigenstates.

Configuration I (see also the discussions in the next subsection and Fig. 2) corresponds to the case in which each electron has a distinct transition frequency between its ground and first excited states. The correlations between the two electrons are then minimal, and the state of the electrons can be controlled, i.e., to perform single-qubit gate operations and readout, independently via their associated resonators using cQED techniques [63]. We focus on cases in which the frequency of the left qubit is larger than that of the right qubit, and within the resonator working range of 5–15 GHz. Then the two-body energy eigenstates $|\Phi_0\rangle$, $|\Phi_1\rangle$, $|\Phi_2\rangle$, and $|\Phi_4\rangle$ have maximum overlap with the Hartree product states $|00\rangle$, $|01\rangle$, $|10\rangle$, and $|11\rangle$, respectively, and we interpret these eigenstates as computational basis states. Because of the minimized correlation, the entanglement entropy is zero for all energy eigenstates of this configuration.

Configuration II is designed to realize the two-qubit $\sqrt{i\text{SWAP}}$ gate. It can be achieved by an avoided crossing of the first and second excited eigenstates, so that they are given by

$$\begin{aligned}|\Phi_1\rangle &= (|10\rangle - |01\rangle)/\sqrt{2},\\ |\Phi_2\rangle &= (|10\rangle + |01\rangle)/\sqrt{2}.\end{aligned} \tag{9}$$

All other energy eigenstates must remain product states to ensure that only $|10\rangle$ and $|01\rangle$ are coupled. The entropy is then 1 for the two states $|\Phi_1\rangle$ and $|\Phi_2\rangle$ and zero for the rest. For a further discussion of avoided level crossings in coupled quantum dot systems, see, for example, Ref. [8].

The presence of higher energy levels gives rise to a different type of correlation between the two electrons

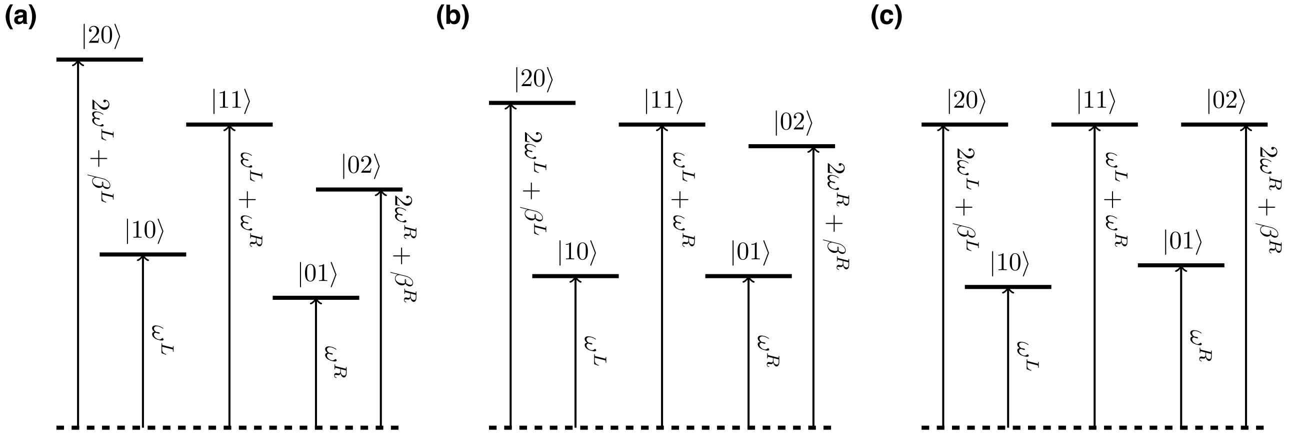

FIG. 2. (a) Transition frequencies in the noninteracting picture for configuration I. This configuration corresponds to a detuned system in which all transition energies are distinguishable, and $\Delta_\text{I} = \omega^L - \omega^R > 0$, with $\beta^L = -\beta^R = \Delta_\text{I}/2$. (b) Transition frequencies in configuration II. Here the detuning is zero, $\Delta_\text{II} = 0$, and the two states $|10\rangle$ and $|01\rangle$ are degenerate in the absence of interactions. Distinct anharmonicities kept at $\beta^L = -\beta^R = \Delta_\text{I}/2$ separate the higher states from one another. (c) Configuration III is realized when the three states $|20\rangle$, $|11\rangle$, and $|02\rangle$ share the same transition frequency from the ground state. This occurs when $\beta^L = -\beta^R = -\Delta_\text{III}$. The detuning has opposite sign of that in configuration I, $\Delta_\text{III} = -\Delta_\text{I}/2$.

in our system. We are particularly interested in a specific type of interaction that enables the realization of a controlled-phase CZ gate [63,88]. Configuration III realizes the conditions to implement this type of two-qubit gate, which involves a “triple” avoided crossing between the third, fourth, and fifth excited eigenstates:

$$|\Phi_3\rangle = (|20\rangle - |02\rangle - \sqrt{2}\,|11\rangle)/2, \qquad (10a)$$

$$|\Phi_4\rangle = (|20\rangle + |02\rangle)/\sqrt{2}, \qquad (10b)$$

$$|\Phi_5\rangle = (|20\rangle - |02\rangle + \sqrt{2}\,|11\rangle)/2. \qquad (10c)$$

The entropies of these states are 1.5, 1, and 1.5, respectively. In this configuration, too, the remaining energy eigenstates must stay as close to their noninteracting counterparts as possible, with entropy close to zero. To quantify the strength of this two-qubit interaction, we define the *ZZ*-coupling strength [86,89,90] (see also the discussions below) as

$$\zeta = E_4 - E_2 - E_1 + E_0. \qquad (11)$$

This quantity measures the shift in transition frequency of one electron when the other electron is excited. The *ZZ* coupling plays an important role in our analysis since it conveys information about the coupling to higher excited states.

In configurations I and II, ζ should be as small as possible to minimize phase errors when driving gates. However, in configuration III the action of the shift can be used to alter the phase of the computational basis state $|\Phi_4\rangle$, which generates the CZ gate [85,88,89].

Tuning the electrode voltages diabatically between configuration I and configuration II or III, the abovementioned two-body quantum gates are realizable [85,88]. Universal two-qubit logic can be performed as follows. We begin with configuration I, where the system is initialized in the ground state and the electrons are decoupled from each other. A single-qubit gate can then be applied to either electron using microwave excitations on corresponding coplanar waveguide resonators, thereby preparing the electrons in specific quantum states. Subsequently, we tune the voltages on the gates to diabatically transition the system to configuration II, allowing the system to evolve for some time to generate entanglement between the two electrons, effectively performing a two-qubit gate operation. Finally, the system is returned to the initial configuration, where the electrons can be further manipulated using single-qubit gates or measured via the corresponding resonators. We proceed to demonstrate that the necessary well configurations and resulting electron entanglement are achievable through targeted numerical optimization. The remainder of this work is focused on the resulting configurations, and we leave actual simulations of time-dependent gate operation to future work.

F. Configurational search

The three desirable well configurations defined in the previous section can be targeted through numerical optimization methods, with the seven electrode voltages as the variational parameters. To achieve the avoided crossings described above, we can use the fact that the Hartree product basis incorporates much of the Coulomb interaction between the electrons, so that the residual Coulomb interaction term is small. This means that the energy spectrum of the full interacting system should be close to the spectrum of Hartree product states [91] $|ij\rangle$, with transition energies given by the sum of the corresponding Hartree transition energies $\epsilon_i^L - \epsilon_0^L + \epsilon_j^R - \epsilon_0^R$ (where the ϵ_i^A are the eigenvalues of the Hartree states as defined in Appendix C). This approximation matches the interacting spectrum well except at the avoided crossings, where the interaction turns what would have been an energy crossing in the noninteracting case into an avoided crossing in the interacting case. In other words, we can look at the Hartree energies of the system and target degenerate Hartree energies to find avoided crossings.

We also target qubit anharmonicities of equal magnitude but opposite sign throughout all three configurations. This was shown to suppress the unwanted *ZZ* coupling defined in Eq. (11) for superconducting qubits [88–90], and so we investigate if the same principle is applicable to our charge qubits. The anharmonicity of each qubit can again be defined through the Hartree energies, which serve as a noninteracting, single-particle guiding picture throughout this section.

Figure 2 illustrates the noninteracting energy spectra of the three target configurations. The transition frequency from $|0\rangle$ to $|1\rangle$ for subsystem $A \in \{L, R\}$ is denoted by $\epsilon_1^A - \epsilon_0^A = \omega^A$ (with $\hbar = 1$). In order to selectively address the ground and first excited energy eigenstates while avoiding population of higher states, the electrostatic potential is intentionally designed to be anharmonic. We define the *anharmonicity* to be the difference in the excitation energy between $|0\rangle \rightarrow |1\rangle$ and $|1\rangle \rightarrow |2\rangle$. Consequently, the transition frequency for $|0\rangle \rightarrow |2\rangle$ is given by $\epsilon_2^A - \epsilon_0^A = 2\omega^A + \beta^A$, where β^A is the anharmonicity.

The energy of the noninteracting Hartree product state $|ij\rangle$ is given by $\epsilon_{ij} = \epsilon_i^L + \epsilon_j^R$. We refer to the difference in energy between states $|10\rangle$ and $|01\rangle$ as the qubit *detuning*, and denote it by $\Delta \equiv \omega^L - \omega^R$. Using the detuning and the anharmonicity, we can express the transition frequencies for $|11\rangle \rightarrow |20\rangle$ and $|02\rangle \rightarrow |11\rangle$ by $\epsilon_{20} - \epsilon_{11} = \Delta + \beta^L$ and $\epsilon_{11} - \epsilon_{02} = \Delta - \beta^R$.

Figure 2(a) illustrates the noninteracting energy spectrum for configuration I. In this configuration all transition frequencies are distinct, and we have chosen a detuning of $\Delta_{\rm I} = \omega^L - \omega^R > 0$ so that the electron in the left well has higher transition frequencies than the electron in the right well. Furthermore, we have set $\beta^L = -\beta^R = \Delta_{\rm I}/2$ such that $\Delta + \beta^L = \Delta - \beta^R > \Delta$, i.e., the energy gaps between $|20\rangle$ and $|11\rangle$, and $|11\rangle$ and $|02\rangle$ are equally large, and greater than the detuning.

Figure 2(b) shows the target noninteracting energy spectrum for configuration II. In this configuration the single-particle basis states $|01\rangle$ and $|10\rangle$ are degenerate, while the higher states $|20\rangle$, $|11\rangle$, and $|02\rangle$ are kept separate from each other. This implies that $\Delta_{\mathrm{II}} = \omega^L - \omega^R = 0$, and we have maintained the anharmonicities at the same values as in configuration I, i.e., $\beta^L = -\beta^R = \Delta_{\mathrm{I}}/2$.

Finally, Fig. 2(c) shows the target noninteracting energy spectrum for configuration III. In this configuration the higher states $|20\rangle$, $|11\rangle$, and $|02\rangle$ are degenerate, while $|10\rangle$ and $|01\rangle$ are distinct. To realize this configuration, we require $\Delta + \beta^L = \Delta - \beta^R = 0$, and with $\beta^L = -\beta^R$ we find that $\beta^L = -\Delta$. Keeping the anharmonicities of the two wells the same as in configurations I and II, i.e., $\beta^L = -\beta^R = \Delta_{\mathrm{I}}/2$, leads to $\Delta_{\mathrm{III}} = -\Delta_{\mathrm{I}}/2$.

The residual Coulomb interaction between the electrons splits the degeneracy in energy levels and leads to avoided level crossings, entanglement between the two electrons, and hence the possibility of driving two-qubit gates. The anharmonicities being nonzero, with equal magnitude and opposite sign also ensure that the avoided crossing between the first and second excited states and the triple avoided crossing between the higher states are separated [88,89].

We note, as indicated in Figs. 2(a) and 2(c), that the detunings in configuration I and configuration III have opposite signs. This is not incidental, but has a deliberate purpose; it allows for the realization of configuration II somewhere in the transitional region between configurations I and III, as long as the anharmonicities have a magnitude greater than zero along the same path. This happens because the detuning has to change sign in order to go from configuration I to configuration III, leading to the characteristic level crossing of configuration II when the detuning is zero. Hence, our task simplifies to locating configurations I and III with equal anharmonicities by tuning the electrode voltages. We can then define a parametrization that interpolates between these two configurations, and as long as the anharmonicities do not go to zero, we are guaranteed to get a configuration II somewhere along the parametrization path.

III. RESULTS AND DISCUSSION

We start this section by summarizing the numerical optimization procedure that was used to locate the above-defined configurations I and III in the parameter space of seven electrode voltages. We then define a parametrization of the voltages and identify the location of configuration II. Thereafter we discuss the properties of each configuration in more detail. Finally, we make an attempt at interpreting our results in terms of a phenomenological model.

A. Configurational results

To find the electrode voltages corresponding to configurations I and III, we express the search as an optimization problem by defining cost functions whose minima align with the desired properties for each configuration, as described in Sec. II F. Each cost function was minimized by evaluating its gradient with respect to the voltages. The optimization of the cost functions was done using standard gradient descent methods with the so-called ADAM algorithm [92] for the gradient updates. As is common in the optimization of multiparameter functions, we found that our cost functions often exhibit several local minima, a feature that makes our solution dependent on the initial guess for the voltages. Because of this, our approach involved manually adjusting the voltages to obtain an initial well configuration resembling a double-well trap with features close to the desired properties, and then running the optimization search. Appendix G provides an in-depth discussion of the full optimization process, including specific expressions for the cost functions.

For configuration I, this procedure successfully achieves distinct transition frequencies of each well, within the resonator working range of 5–15 GHz. We also target anharmonicities with equal magnitude and opposite signs to suppress *ZZ* crosstalk in higher-energy states, as discussed in Sec. II F. However, an arbitrary choice of transition frequencies and anharmonicities does not necessarily result in an appropriate well configuration. By performing the optimization process for a range of possible candidates, we ended up targeting the specific transition frequency of $\omega^L/2\pi = 11\,\mathrm{GHz}$ between the two lowest-energy levels in the left well, and a transition frequency of $\omega^R/2\pi = 9\,\mathrm{GHz}$ in the right well. This corresponds to a detuning of $\Delta_{\mathrm{I}}/2\pi = (\omega^L - \omega^R)/2\pi = 2\,\mathrm{GHz}$. At the same time, anharmonicities of $\beta^L/2\pi = -\beta^R/2\pi = (\Delta_{\mathrm{I}}/2)/2\pi = 1\,\mathrm{GHz}$ were targeted. Optimization of the cost function based on these target values [Eq. (G1) in Appendix G] yields properties that are very close to the desired ones. The two-body energies of the resulting configuration are $E_1/2\pi = 8.99\,\mathrm{GHz}$ and $E_2/2\pi = 11.01\,\mathrm{GHz}$ relative to the ground state, and the anharmonicities are equal to the targeted values of $\pm 1\,\mathrm{GHz}$ to three decimal places.

For configuration III, we achieve a triple degeneracy point between the computational basis state $|11\rangle$ and states $|20\rangle$ and $|02\rangle$. Here we construct a cost function targeting the entropies of the energy eigenstates $|\Phi_3\rangle$, $|\Phi_4\rangle$, and $|\Phi_5\rangle$ to be 1.5, 1.0, and 1.5, respectively, while keeping the entropies of all other eigenstates small. In addition, we target the detuning $\Delta_{\mathrm{III}}/2\pi$ to be $-1\,\mathrm{GHz}$ and the same anharmonicities as for configuration I, $\beta^L/2\pi = -\beta^R/2\pi = 1\,\mathrm{GHz}$. As discussed earlier, this guarantees the presence of configuration II for a certain set of voltages in the transition from configuration I to configuration III. We use the set of voltages obtained for configuration I as an initial guess for the optimization of this cost function [Eq. (G2) in Appendix G]. This optimization results in two-body energies $E_3/2\pi = 27.24$ GHz, $E_4/2\pi = 27.42$ GHz, and $E_5/2\pi = 27.61$ GHz relative to the ground state, with entropies of 1.50, 1.00, and 1.49, respectively.

To visualize properties of the configurations and the tuning between them, we express the seven electrode voltages with one configuration parameter λ, through a linear parametrization

$$\mathbf{V}(\lambda) = (1-\lambda)\mathbf{V}_{\mathrm{I}} + \lambda\mathbf{V}_{\mathrm{III}}. \tag{12}$$

Here, $\mathbf{V}_{\mathrm{I}}$ and $\mathbf{V}_{\mathrm{III}}$ are vectors with the optimized voltages for configurations I and III. By construction, configuration I then corresponds to $\lambda = 0$, while configuration III corresponds to $\lambda = 1$. Explicit values of the voltages for each optimized configuration are provided in Table I in Appendix H.

Figure 3 shows CI results for the two-body energy spectrum for the five lowest excited states, the corresponding entanglement entropies, as well as the anharmonicities and detuning of the wells as a function of the configurational parameter λ. Two avoided crossings are clearly observed in the spectrum in Fig. 3(a): a triple avoided crossing at $\lambda = 1$ between the three highest-energy states, and an avoided crossing between the two first excited states at $\lambda \approx 0.46$, corresponding to configuration II. In the latter case we extract the coupling strength of $g_{\mathrm{CI}} \approx 113$ MHz from the energy gap at the location of the avoided crossing. This will be discussed in more detail in Sec. III B below.

Qualitatively, the impact of the Coulomb interaction on the system's electrons can be understood in two steps. First, the electric field created by one electron alters the potential energy experienced by the other electron. This results in a modified effective potential trap, which gives rise to the Hartree product states and their associated energies. These noninteracting energies are depicted by the dashed lines in the insets of Fig. 3(a). Second, in the case of a voltage configuration that results in two or more Hartree product states with the same energies, the residual Coulomb interaction between the electrons lifts the degeneracy and leads to an energy gap between the corresponding two-body energy eigenstates, resulting in the abovementioned avoided crossings. Far from the point of degeneracy, the Hartree product states provide a good description of the full two-body energy eigenstates. This can be observed, for example, in configuration I at $\lambda = 0$. In these configurations, the calculated entropy values S_n demonstrate minimal values, indicating reduced correlations between the electrons. The entropy values reach their maximum and align with theoretical values precisely at the locations of the avoided crossings, as illustrated in Fig. 3(b).

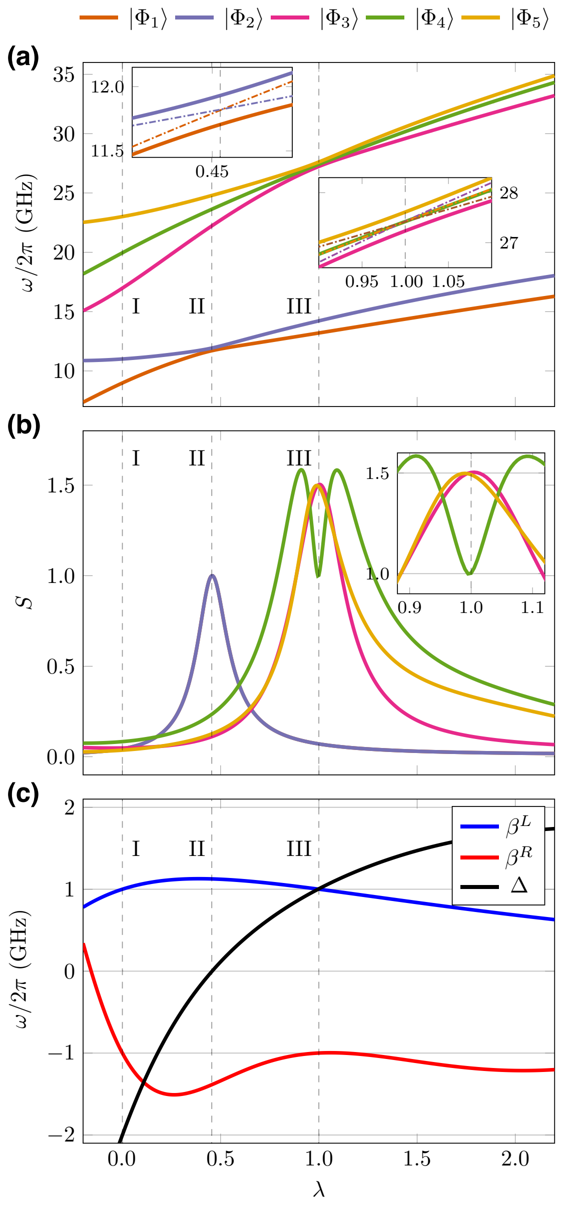

FIG. 3. (a) Transition frequencies from the ground state of the five lowest excited energy eigenstates, as a function of the configurational parameter λ. Solid lines correspond to the transition energies of the full Hamiltonian. In the insets we have included thin dashed lines for the transition energies of the noninteracting Hartree product states. (b) Von Neumann entropies of the same five eigenstates as functions of the configurational parameter λ. The entropy is calculated with the binary (base-2) logarithm. (c) Anharmonicities of the left (β^L) and right (β^R) wells as a function of the configurational parameter λ, as well as the detuning $\Delta = \omega^R - \omega^L$ between the two wells. Marked in all subfigures are configurations I, II, and III at their respective λ values of 0, 0.46, and 1.

A triple avoided crossing is observed in the higher-energy states in configuration III at $\lambda = 1$, and arises due to the opposite signs of the anharmonicities [see Fig. 3(c)]

[88]. It is worth mentioning that the anharmonicities vary across different values of λ since the linear interpolation of the voltages does not guarantee that the properties of the system also behaves linearly.

The two-body coefficients $C_{ij,n}$ corresponding to the six lowest-energy eigenstates, as defined in ansatz (6), are depicted in Fig. 4 for the three main configurations. These coefficients demonstrate a good convergence of our optimization algorithm towards the target wave functions presented in Eqs. (9) and (10). In configuration I, the two-body eigenstates are effectively described by single Hartree product states, indicating the suppression of electron-electron correlations when the potential wells are detuned. In contrast, the coefficients $C_{ij,n}$ for configurations II and III reveal a high degree of entanglement, which is quantified using von Neumann entropies. A closer inspection of these coefficients reveals the presence of small, undesired Hartree terms in the two-body wave functions. For instance, for the first excited state in configuration I, shown in Fig. 4(a), we find that

$$|\Phi_1\rangle_{\mathrm{I}} \approx \sqrt{0.995}\,|01\rangle + \sqrt{0.005}\,|10\rangle \tag{13}$$

with a corresponding entropy of $S_1 \approx 0.04$. Furthermore, we find a small mixing in states $|\Phi_3\rangle$, $|\Phi_4\rangle$, and $|\Phi_5\rangle$, indicating residual correlations between the two electrons through interactions with higher-energy states. The degree of these remaining correlations, quantified by the entropies S_n, show small but nonzero values for all excited energy states. The underlying factors contributing to these observations will be discussed within the framework of the effective Hamiltonian model presented in the following subsection.

For the first two excited states in configuration II, shown in Fig. 4(b), the many-body wave functions are approximately described by

$$\begin{aligned} |\Phi_1\rangle_{\mathrm{II}} &\approx \sqrt{0.513}\,|01\rangle - \sqrt{0.487}\,|10\rangle\,, \\ |\Phi_2\rangle_{\mathrm{II}} &\approx \sqrt{0.487}\,|01\rangle + \sqrt{0.513}\,|10\rangle\,, \end{aligned} \tag{14}$$

which are almost identical to the maximally entangled states in Eq. (9). The entropy for these entangled states reach a maximum value of 1, as seen in Fig. 3(b). Here too, none of the higher excited states can be entirely described by single product states, indicating the presence of small residual correlations. The entropies of the eigenstates $|\Phi_3\rangle$, $|\Phi_4\rangle$, and $|\Phi_5\rangle$ for configuration II are around 0.11, 0.23, and 0.13, respectively.

We display the coefficients of the energy eigenstates for configuration III in Fig. 4(c). The three states involved in the triple avoided crossing are close to the target states

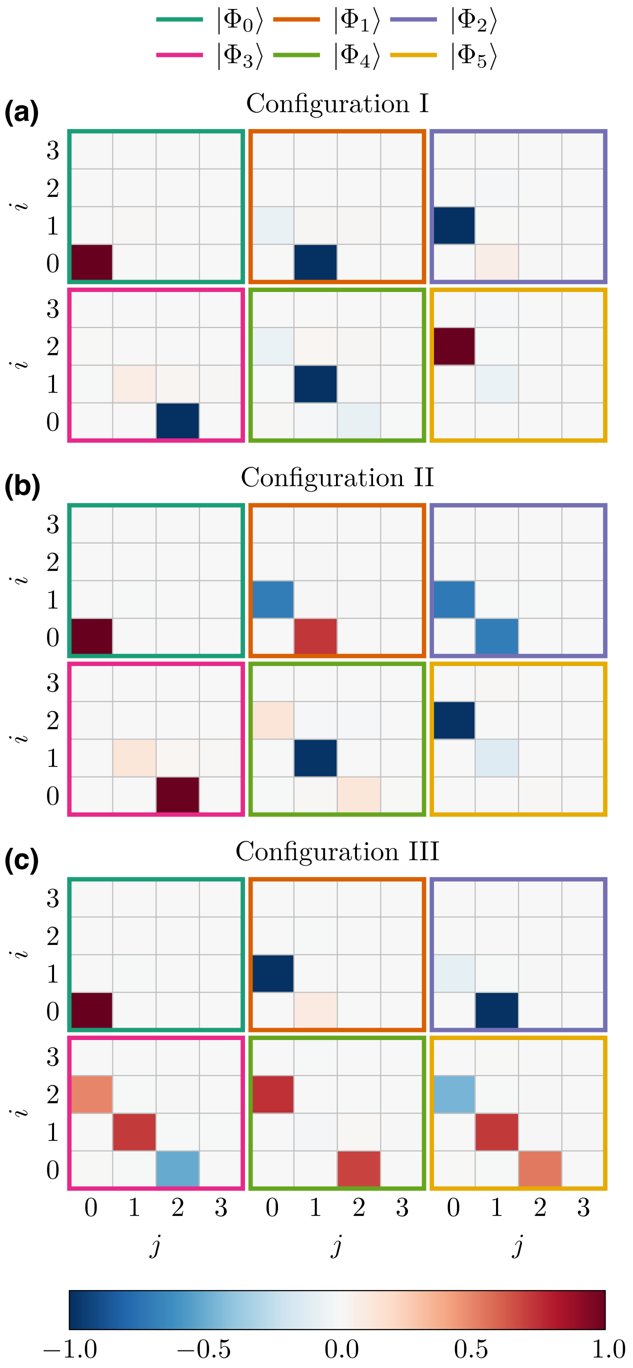

FIG. 4. Two-body wave-function coefficients $C_{ij,n}$ of the six lowest-energy eigenstates for each configuration, as defined in Eq. (6). The indices on the x and y axes correspond to the Hartree product states involved with each coefficient, so that the coefficient at tile (i, j) is multiplied with the product state $|\phi_i^L \phi_j^R\rangle$ and summed into the expansion of each energy eigenstate. (a) Coefficients for configuration I. Each energy eigenstate is well approximated by a single Hartree product state. (b) Coefficients for configuration II. The first and second excited eigenstates are close to maximally entangled. (c) Coefficients for configuration III. Here, the third, fourth, and fifth excited eigenstates are entangled.

given in Eqs. (10):

$$|\Phi_3\rangle_{\text{III}} \approx -\sqrt{0.259}\,|02\rangle + \sqrt{0.244}\,|20\rangle + \sqrt{0.497}\,|11\rangle\,,$$
$$|\Phi_4\rangle_{\text{III}} \approx \sqrt{0.461}\,|02\rangle + \sqrt{0.538}\,|20\rangle - \sqrt{0.001}\,|11\rangle\,,$$
$$|\Phi_5\rangle_{\text{III}} \approx \sqrt{0.279}\,|02\rangle - \sqrt{0.218}\,|20\rangle + \sqrt{0.502}\,|11\rangle\,.$$

In this configuration, however, an unwanted coupling is present in the first and second excited eigenstates $|\Phi_1\rangle$ and $|\Phi_2\rangle$. The degree of entanglement for these states is rather weak, with entropies of around 0.07, as shown at $\lambda = 1$ in Fig. 3(b).

We note that Fig. 4 demonstrates that the Hartree states serve as approximate Schmidt states for all the energy eigenstates of our system, as mentioned in Sec. II D. This is clearly seen from this figure since each row and column only have one approximately nonzero coefficient.

For the sake of visualization, we include in Appendices C and F the probability distributions of the one-body Hartree basis states (Fig. 6) and the particle densities of the two-body energy states (Fig. 7) for each of the three configurations.

B. Effective Hamiltonian

In addition to the numerical results above, we present a simplified model of the system to provide an intuitive understanding of the underlying coupling mechanism between the two electrons. For this purpose, we expand both the electrostatic potential terms and the Coulomb interaction in our model Hamiltonian [Eq. (3)] around equilibrium positions x_L and x_R for the two electrons. These equilibrium positions are defined so that the first-order terms in the displacements Δx_i cancel each other, leaving only terms of second order and higher.

The Taylor expansion of the electrostatic potential around the equilibrium positions results in harmonic traps $\omega_i^2 \Delta x_i^2/2$, with frequencies defined by the curvature of the electrostatic potential at the equilibrium positions. The Coulomb interaction between the two electrons can also be expanded in terms of the displacements Δx_i. Considering only up to second-order terms we obtain

$$\frac{\kappa}{|x_1 - x_2|} \approx \frac{\kappa}{d}\left(1 - \frac{\Delta x_1 - \Delta x_2}{d} + \frac{(\Delta x_1 - \Delta x_2)^2}{d^2}\right), \tag{15}$$

where $d = x_R - x_L$ is the distance between the two electrons in equilibrium. The total potential energy of the system in displacement-dependent terms takes the form

$$U_{\text{C}} \approx \sum_{i=1,2} \frac{\omega_i^2 + \omega_{\text{C}}^2}{2}\Delta x_i^2 + \omega_{\text{C}}^2 \Delta x_1 \Delta x_2, \tag{16}$$

where $\omega_{\text{C}}^2 = 2\kappa/d^3$. The first term in this equation describes how the Coulomb interaction effectively modifies the potential wells from the electrostatic potential. This is similar to the Hartree method since it computes an effective mean potential for each electron, created by the other electron in the system; however, it is also different in that it treats the electrons as point particles instead of quantum particles. The last term in Eq. (16) gives rise to correlations between the two electrons. By introducing canonical transformations for the displacements and applying the rotating-wave approximation, the Hamiltonian of the system takes the form

$$\hat{H} \approx \omega^L \hat{a}^\dagger \hat{a} + \omega^R \hat{b}^\dagger \hat{b} + g(\hat{a}^\dagger \hat{b} + \hat{a}\hat{b}^\dagger), \tag{17}$$

where $\hat{a}$ and $\hat{b}$ are ladder operators of displacement in the left and right wells, respectively, $(\omega^L)^2 = \omega_1^2 + \omega_{\text{C}}^2$ and $(\omega^R)^2 = \omega_2^2 + \omega_{\text{C}}^2$ are modified vibrational frequencies, and $g = \omega_{\text{C}}^2/2\sqrt{\omega^L\omega^R}$ describes the interaction strength.

This Hamiltonian is diagonalized by a standard Bogoliubov transformation $U_\theta = \exp[\theta(\hat{a}^\dagger\hat{b} - \hat{a}\hat{b}^\dagger)]$ with a rotation angle $2\theta = \arctan(2g/\Delta)$ [63]. The resulting Hamiltonian takes the diagonal form $\hat{H} = \Omega^+\hat{\alpha}^\dagger\hat{\alpha} + \Omega^-\hat{\beta}^\dagger\hat{\beta}$. The $\hat{\alpha}$ and $\hat{\beta}$ are transformed ladder operators, and the eigenfrequencies of the corresponding hybridized modes are given by

$$\Omega^\pm = \frac{1}{2}\left(\omega^L + \omega^R \pm \sqrt{4g^2 + \Delta^2}\right). \tag{18}$$

Here $\Delta = \omega^L - \omega^R$ is the detuning between the two wells, as defined in Sec. II F.

Given the multilevel nature of electronic states in each well, one has to carefully treat the unitary transformation of the effective Hamiltonian in Eq. (17). Including the anharmonicity of each oscillator as additional terms $\beta^L\hat{a}^\dagger\hat{a}(\hat{a}^\dagger\hat{a} - 1)/2$ and $\beta^R\hat{b}^\dagger\hat{b}(\hat{b}^\dagger\hat{b} - 1)/2$ in the Hamiltonian, which corresponds to including quartic terms in the expansion of the electrostatic potential, results in correlations emerging from interactions between the higher-energy states. After performing a Bogoliubov transformation U_θ similar to that above, the term corresponding to the anharmonicities takes the form

$$\hat{H}_{ZZ} = \frac{\zeta}{2}\hat{\alpha}^\dagger\hat{\alpha}\hat{\beta}^\dagger\hat{\beta}, \tag{19}$$

where ζ is given by

$$\zeta = \sqrt{2}g\left(\tan\frac{\theta_R}{2} - \tan\frac{\theta_L}{2}\right) \tag{20}$$

with $\tan\theta_{L/R} = 2\sqrt{2}g/(\Delta \pm \beta^{L/R})$ [88]. The quantity ζ corresponds to the energy shift defined in Eq. (11), and is

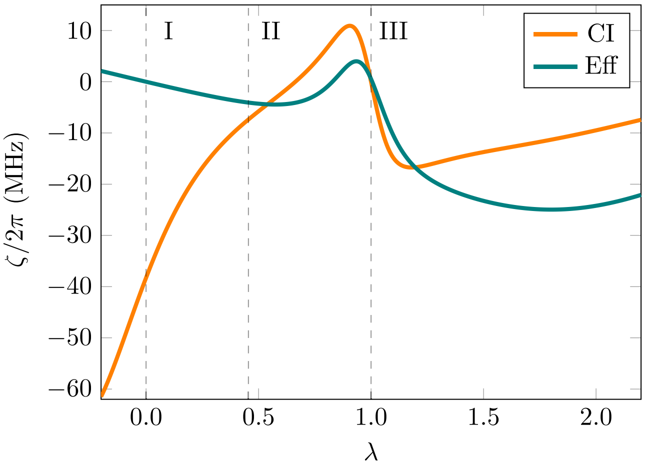

FIG. 5. The energy difference ζ defined in Eq. (11). The orange line represents results from the numerical solution of the full two-body problem, whereas the teal line shows ζ values calculated from the effective Hamiltonian approach. Frequencies obtained from Hartree energies and a fixed coupling strength determined at the avoided crossing of configuration II were used in the effective model calculations. Configurations I, II, and III are marked with vertical dashed lines at their respective λ values of 0, 0.46, and 1.

the result of interactions between the $|20\rangle$ and $|02\rangle$ states and the $|11\rangle$ state.

In general, unwanted correlations from this type of interaction lead to a conditional phase accumulation on the electron's states, as discussed in Sec. II E. In Fig. 5 we show calculations of ζ from our CI calculations and from the effective Hamiltonian approach. In the framework of the effective Hamiltonian this quantity strongly depends on the relative signs of the anharmonicities, which can be seen from expression (20). For small $\theta_{L/R} \ll 1$ values, which are realized in configuration I, the coupling strength can be approximated by $\zeta \approx 2g^2/(\Delta + \beta^L) - 2g^2/(\Delta - \beta^R)$. This vanishes at equal but opposite sign anharmonicities of two electrons. However, the CI calculations show a strong deviation of ζ from the predictions based on the effective model for well configurations $\lambda < 0.5$ and $\lambda > 1.5$ (see Fig. 5). We argue that these residual correlations appear due to a complexity in the shape of the potential wells. Nonlinearities on the localization length scale of electrons requires us to include higher-order terms in the Taylor expansion of the electrostatic and Coulomb potentials. These terms, together with the anharmonicities, can change for different voltage configurations, a feature which further complicates our model. These intricacies are inherent to the electrostatic field generated by the array of electrodes in the microdevice considered. Potentially, the *ZZ*-coupling strength can be included in the configurational search as another minimization parameter to further suppress such correlations between the two electrons.

The effective Hamiltonian presented in Eq. (17) represents one of the most elementary models for describing coupled two-qubit systems. This model finds widespread use in various superconducting qubit architectures. Its simplicity in form facilitates the mapping of diverse entangling gates from these platforms to our system. However, alongside the simplicity of this model, we have illustrated its limitations when comparing its predictions with the results of full CI calculations. These limitations need to be handled thoughtfully in order to account for all potential sources of entanglement. Addressing these limitations becomes crucial for providing an accurate and complete description of the entanglement dynamics within the system and will be the scope of future work.

IV. CONCLUSIONS

The results presented in this work highlight how the Coulomb interaction can induce motional entanglement between electronic states localized in separate wells above the surface of superfluid helium. To find the optimal specific device parameters for generating the entangled states, we have developed an optimization method based on many-body methods like full CI theory [62] together with effective optimization algorithms. Our optimization methodology allows us to determine the optimal voltage configuration on the device electrodes needed to generate entanglement. In this way, the many-body-physics-based methodology we have developed has the potential to serve as a valuable tool to guide experimental work and inform future device design.

As an illustration, in this work we examined three distinct device parameter configurations (I, II, and III), leading to different types of entanglement between the two electrons. The tunability of the microdevice allows us to adjust the applied voltages and dynamically create highly anharmonic electrostatic traps, even with varying signs of anharmonicity. This tunability offers precise control over the potential landscape experienced by the electrons and allows for the tailoring of trapping potentials for specific experimental requirements, such as the experimental realization of specific gates and operations on the electronic qubits. Additionally we employed an effective Hamiltonian to approximate the two-electron system, which was in turn compared with our exact CI calculations, allowing us to investigate the limitations of the approximations used to construct this effective model. This comparison holds promise for a more detailed understanding of errors in the simulation of quantum devices based on this trapped electron system.

Finally, recent theoretical investigations have explored the dynamics and decoherence of electron spins above the surface of liquid helium [46]. These studies considered the role of spin-orbit interactions, which can be artificially enhanced by applying a spatially inhomogeneous magnetic field parallel to the helium surface. In future studies the methodology developed in our work can be extended to investigate entangling interactions between spins, devices containing spatially varying magnetic fields, as well as dynamical driving fields to investigate the time dependence of entangled charge states and spin states.

In addition to studies of the time evolution of these quantum-mechanical systems and thereby the temporal evolution of entangled states, we plan to extend our studies to more than two particles, with the aim to explore the experimental realization of many-body entanglement for electrons above the surface of liquid helium and solid neon. Using the Coulomb interaction, as demonstrated in this work, to facilitate entanglement between motional states, one could consider a linear chain of electrons trapped in a long microchannel filled with liquid helium. Experimental realizations of single chains of electrons with up to several hundred electrons have been demonstrated in 100-μm-long channels [50]. In this setup, each electron can be controlled by its own individual electrodes beneath the helium surface, similar to the system studied in this work. Such a scaling up of the system to more electrons in a linear chain resembles to a large extent linear ion trap architectures. In a similar way, the interaction between electrons can be mediated by Coulomb interaction-driven motional modes of the linear chain, thereby allowing for an upscaling of the system.

The hope is that these theoretical tools can guide studies of entanglement, development of experimental devices, and realization of quantum gates and circuits for systems of many trapped and interacting electrons.

ACKNOWLEDGMENTS

We are grateful to M.I. Dykman, S.A. Lyon, and M. Sammon for illuminating discussions. The work of M.H.-J. is supported by the U.S. Department of Energy, Office of Science, Office of Nuclear Physics under Grant No. DE-SC0021152 and U.S. National Science Foundation Grants No. PHY-1404159 and No. PHY-2013047. J.P. acknowledges support from the National Science Foundation via Grant No. DMR-2003815 as well as the valuable support of the Cowen Family Endowment at MSU. A.K.W. acknowledges support from the U.S. Department of Energy, Office of Science, Basic Energy Sciences, Grant No. DE-SC0017889, and support from MSU for a John A. Hannah Professorship. The work of N.R.B. was supported by a sponsored research grant from EeroQ Corp. J.P. and N.R.B. additionally thank J.R. Lane and J.M. Kitzman for illuminating discussions. O.L. received funding from the European Union's Horizon 2020 research and innovation program under the Marie Skłodowska-Curie Grant Agreement No. 945371.

APPENDIX A: ELECTRON-RIPPLON COUPLING HAMILTONIAN

The coupling of the electron to the surface deformations (ripplons) is described with Hamiltonian

$$H_i = eE\xi(\mathbf{r}), \tag{A1}$$

where $\xi(\mathbf{r})$ is the helium surface displacement and E is the normal component of the total electric field, which includes both the field produced by the trapping electrodes as well as a polarization term due to a change of the helium surface curvature by the electron [40]. To estimate the electron-ripplon coupling energy, we consider only the effect of the externally applied field because, for the typical values of voltages used to create double-well potential, the applied field $E_\perp^{\text{applied}} \approx 10^5$ V/m is larger than the polarization term $E_\perp^{\text{pol}}(q) \approx 2 \times 10^4$ V/m for the ripplon wavelengths $q \sim 1/l_x$ (where l_x is the electron localization length in the electrostatic trap). The helium surface displacement can be estimated from the thermal average of the squared helium surface fluctuations $\delta_{\text{th}} = \sqrt{\langle \xi^2 \rangle_{\text{th}}}$. The helium surface displacement is related to the creation and annihilation operators of ripplons by

$$\xi(\mathbf{r}) = \sum_{\mathbf{q}} \sqrt{\frac{1}{S}\frac{\hbar q}{2\rho\omega_q}} (b_{\mathbf{q}} + b_{-\mathbf{q}}^\dagger) e^{i\mathbf{q}\mathbf{r}}, \tag{A2}$$

where $b_{\mathbf{q}}^\dagger$ and $b_{\mathbf{q}}$ are the ripplon creation and annihilation operators, respectively, $\omega_q = \sqrt{\alpha/\rho \cdot q^3}$ is the ripplon dispersion relation with helium surface tension $\alpha = 3.7 \times 10^{-4}$ N/m and density $\rho = 145$ kg/m^3, and S is the area of the liquid helium surface. At $T = 20$ mK a characteristic value for these thermal fluctuations is $\delta_{\text{th}} \simeq 0.2$ pm. With these estimates we find that $\langle H_i \rangle / \hbar\omega_e \approx 10^{-3}$. Ripplons, being relatively soft excitations, cause slow electron relaxation due to limited momentum transfer ($\hbar q \lesssim \hbar l_x^{-1}$) during scattering processes. The energy of ripplons with this momentum is much lower than the electron level spacing $\hbar\omega_e$ in the double dots. Transitions between electron orbital states, which are of the order of 5–15 GHz, require emitting or absorbing two ripplons. The coupling of the electron to these excitations is weak, resulting in long electron orbital lifetimes, estimated to be around 0.1 ms [40,46], and therefore we ignore the electron-ripplon interaction in our model Hamiltonian.

APPENDIX B: CONSTRUCTING THE SINGLE-PARTICLE BASIS SETS

For our numerical calculations, we use a pseudospectral basis, i.e., a discrete variable representation (DVR), and adopt a linear interpolation for the coupling constants $\alpha_i(x)$. Specifically, we use the one-dimensional sinc-DVR basis suggested by Colbert and Miller [93]. After dividing the Hamiltonian into two distinguishable subsystems L and R, as shown in Eq. (5), we establish two sinc-DVR basis sets, one for each well. We denote these basis functions by $B^A = \{\chi^A_\alpha(x) \mid \alpha = 0, \ldots, K^A\}$ with the corresponding quadrature of collocation points and weights $Q^A = \{(x^A_\alpha, w^A_\alpha) \mid \alpha = 0, \ldots, K^A\}$ for $A \in \{L, R\}$. The quadrature is uniform for the sinc-DVR basis, meaning that $w^A_\alpha = \Delta x^A$ and $x^A_{\alpha+1} = x^A_\alpha + \Delta x^A$ for all α.

We let $x^L_{K^L+1} = x_b = x^R_0$, i.e., the barrier is only included as a quadrature point in the right system, and we let $\Delta x = \Delta x^L = \Delta x^R$. The sinc-DVR functions are then given by

$$\chi^A_\alpha(x) = \frac{1}{\sqrt{\Delta x}} \operatorname{sinc}\left(\frac{x - x^A_\alpha}{\Delta x}\right)$$

with

$$\operatorname{sinc}(x) = \begin{cases} \dfrac{\sin(\pi x)}{\pi x}, & x \neq 0, \\ 1, & x = 0. \end{cases}$$

This means that $\chi^A_\alpha(x^A_\beta) = (\Delta x)^{-1/2}\delta_{\alpha\beta}$ on the quadrature. By restricting the grid on each side only up to the barrier, we have effectively established an infinite potential wall. This means that the potentials given in Eqs. (4) are altered to

$$v^L(x) = \begin{cases} v(x), & x < x_b, \\ \infty, & x \geq x_b, \end{cases}$$

$$v^R(x) = \begin{cases} \infty, & x < x_b, \\ v(x), & x \geq x_b. \end{cases}$$

This forces each electron to remain in its own well, and might seem an extreme limitation. However, the results in our model are completely unchanged, and it is much more computationally efficient and practical to use two separate basis sets.

The matrix elements of the kinetic energy operator are given by [93]

$$t^A_{\alpha\beta} = \langle \chi^A_\alpha | -\frac{1}{2}\frac{\mathrm{d}^2}{\mathrm{d}x^2} | \chi^A_\beta \rangle = \begin{cases} \dfrac{\pi^2}{6(\Delta x)^2}, & \alpha = \beta, \\ \dfrac{(-1)^{\alpha-\beta}}{(\Delta x)^2(\alpha-\beta)^2}, & \alpha \neq \beta, \end{cases}$$

and the external potential is approximated using the quadrature rule, viz.,

$$\begin{aligned} v^A_{\alpha\beta} &= \langle \chi^A_\alpha | \hat{v}^A(x) | \chi^A_\beta \rangle \\ &\approx \Delta x \sum_{\gamma=0}^{K^A} \chi^A_\alpha(x^A_\gamma) v^A(x^A_\gamma) \chi^A_\beta(x^A_\gamma) = \delta_{\alpha\beta} v^A(x^A_\beta), \end{aligned}$$

that is, the potential is diagonal. The matrix elements of the full one-body Hamiltonian can then be written as

$$h^A_{\alpha\beta} = t^A_{\alpha\beta} + \delta_{\alpha\beta} v^A_\beta,$$

where we have defined the diagonal potential matrix elements $v^A_\beta \equiv v^A(x^A_\beta)$.

To evaluate the two-body Coulomb interaction, we examine the matrix elements of tensor products of DVR states., i.e., $|\chi^L_\alpha \chi^R_\beta\rangle = |\chi^L_\alpha\rangle \otimes |\chi^R_\beta\rangle$. We also use the convention that $\langle \chi^L_\alpha \chi^R_\beta| = \langle \chi^L_\alpha| \otimes \langle \chi^R_\beta| = |\chi^L_\alpha \chi^R_\beta\rangle^\dagger$ for the conjugate states. We are able to directly compute the matrix elements of the soft Coulomb interaction operator using the quadrature rule. The matrix elements are thus

$$\begin{aligned} u_{\alpha\beta,\gamma\delta} &= \langle \chi^L_\alpha \chi^R_\beta | \hat{u}(x_1, x_2) | \chi^L_\gamma \chi^R_\delta \rangle \\ &\approx \Delta x^L \Delta x^R \sum_{\sigma=0}^{K^L} \sum_{\tau=0}^{K^R} \chi^L_\alpha(x^L_\sigma) \chi^R_\beta(x^R_\tau) u(x^L_\sigma, x^R_\tau) \\ &\quad \times \chi^L_\gamma(x^L_\sigma) \chi^R_\delta(x^R_\tau) \\ &= \delta_{\alpha\gamma}\delta_{\beta\delta} u(x^L_\gamma, x^R_\delta), \end{aligned}$$

which is diagonal for each particle axis. We label the matrix elements of the diagonal Coulomb operator by $u^{LR}_{\gamma\delta} \equiv u(x^L_\gamma, x^R_\delta)$.

APPENDIX C: THE HARTREE METHOD

In the Hartree method for two distinguishable particles we approximate the ground state $|\Phi_0\rangle$ of the full Hamiltonian $\hat{H}$ in Eq. (2) as the product state $|\Phi_0\rangle \approx |\Psi\rangle = |\phi^L_0 \phi^R_0\rangle$ under the constraint that the Hartree orbitals are orthonormal, i.e., $\langle \phi^A_0 | \phi^A_0 \rangle = 1$. This lets us set up the Lagrangian

$$L = E_H - \lambda^L(\langle \phi^L_0 | \phi^L_0 \rangle - 1) - \lambda^R(\langle \phi^R_0 | \phi^R_0 \rangle - 1),$$

where the λ^A are Lagrange multipliers, and the Hartree energy $E_H = \langle \Psi | \hat{H} | \Psi \rangle$ is given by

$$E_H = \langle \phi^L_0 | \hat{h}^L | \phi^L_0 \rangle + \langle \phi^R_0 | \hat{h}^R | \phi^R_0 \rangle + \langle \phi^L_0 \phi^R_0 | u | \phi^L_0 \phi^R_0 \rangle.$$

Our next objective is to minimize the Lagrangian with respect to the Hartree states and the multipliers. To do this, we expand the Hartree states as a linear combination of sinc-DVR states, i.e.,

$$|\phi^A_i\rangle = \sum_{\alpha=0}^{K^A} B^A_{\alpha i} |\chi^A_\alpha\rangle, \tag{C1}$$

and minimize with respect to the coefficients $B^A_{\alpha i}$. Computing $\partial L/\partial {B^A_{\alpha 0}}^*=0$ gives two coupled eigenvalue equations,

$$\underbrace{\sum_{\beta=0}^{K^L}\left(h^L_{\alpha\beta}+\delta_{\alpha\beta}\sum_{\gamma=0}^{K^R}\left|B^R_{\gamma 0}\right|^2 u^{LR}_{\beta\gamma}\right)}_{\equiv f^L_{\alpha\beta}} B^L_{\beta 0}=\lambda^L B^L_{\alpha 0}, \tag{C2a}$$

$$\underbrace{\sum_{\beta=0}^{K^R}\left(h^R_{\alpha\beta}+\delta_{\alpha\beta}\sum_{\gamma=0}^{K^L}\left|B^L_{\gamma 0}\right|^2 u^{LR}_{\gamma\beta}\right)}_{\equiv f^R_{\alpha\beta}} B^R_{\beta 0}=\lambda^R B^R_{\alpha 0}, \tag{C2b}$$

that need to be solved iteratively until self-consistency has been achieved. The Hartree matrices $f^A_{\alpha\beta}$ are defined as everything inside the parentheses in the equations above. By diagonalizing the Hartree matrices, we obtain K^A eigenvalues and eigenvectors, not just the lowest pair λ^A and $B^A_{\alpha 0}$. We select the N^A+1 lowest eigenvectors, which gives us the set $P^A=\{\left|\phi^A_i\right\rangle \mid i=0,\ldots,N^A\}$, where $N^A \ll K^A$.

The equations we solve are $\hat{f}^{\,A}\left|\phi^A_i\right\rangle=\epsilon^A_i\left|\phi^A_i\right\rangle$, where $\hat{f}^{\,A}$ is the Hartree matrix defined earlier, and the ϵ^A_i are the eigenvalues with the corresponding eigenvectors $\left|\phi^A_i\right\rangle$. These eigenvalues describe the energy felt by a single particle trapped in one of the wells under the influence of a charge in the other well. Formulated in terms of the coefficients, the equations are

$$\sum_{\beta=0}^{K^A} f^A_{\alpha\beta}B^A_{\beta i}=\epsilon^A_i B^A_{\alpha i}$$

with the $f^A_{\alpha\beta}$ the Hartree matrices from Eqs. (C2). These equations are solved iteratively until a convergence of $|\epsilon^{A,(k+1)}_i-\epsilon^{A,(k)}_i|<\delta\epsilon$ with $\delta\epsilon=1\times 10^{-10}$ has been reached. Here k corresponds to an iteration number. We choose ${f^A_{\alpha\beta}}^{(0)}=h^A_{\alpha\beta}$ as an initial state such that

$$\sum_{\beta=0}^{K^A} h^A_{\alpha\beta}B^{A,(0)}_{\beta i}=\epsilon^{A,(0)}_i B^{A,(0)}_{\alpha i}.$$

For the three target configurations found through numerical optimization in this work, the probability distributions of the first four Hartree states in each well are plotted in Fig. 6.

APPENDIX D: FULL CONFIGURATION INTERACTION FOR TWO DISTINGUISHABLE PARTICLES

Once the Hartree equations are solved, we obtain the coefficients $B^A_{\alpha i}$, which allow us to construct the Hartree basis P^A from the sinc-DVR basis B^A using Eq. (C1). We can perform a basis transformation from the sinc-DVR basis to the smaller Hartree basis by using the relations

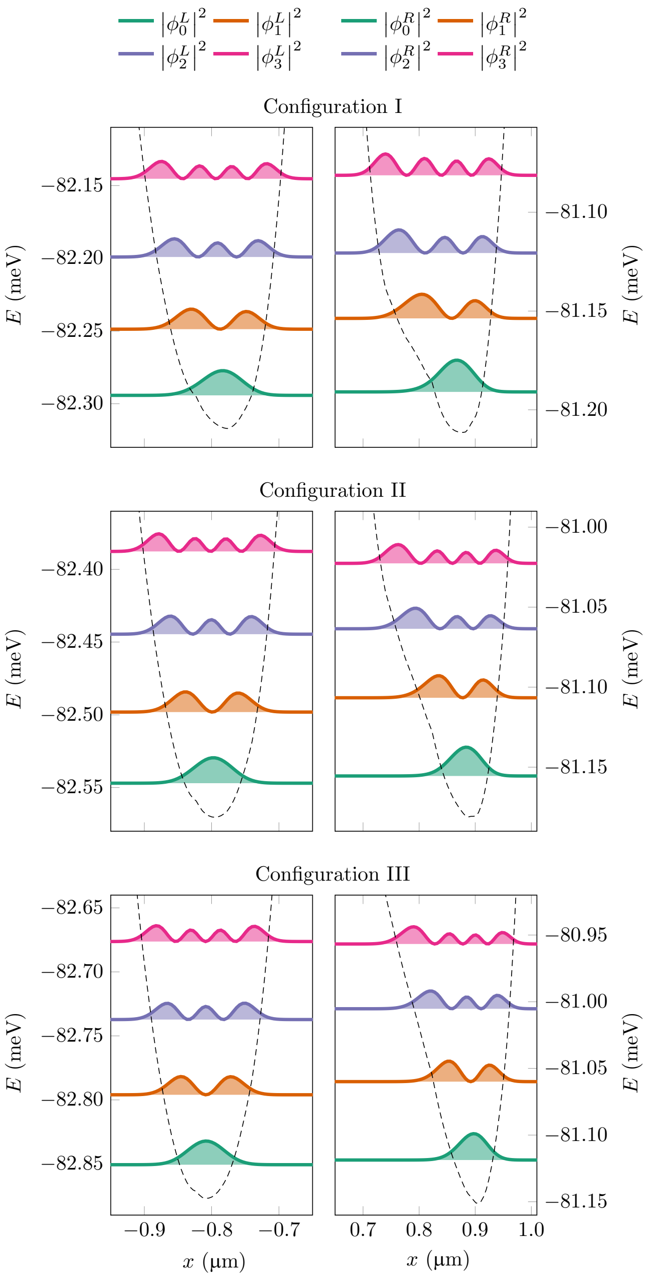

FIG. 6. Probability distributions of the first four Hartree states in the left and right wells for all three configurations. The positions of the distributions are shifted along the y axis to reflect their individual Hartree energy. The effective potentials for each subsystem, i.e., the well potential set up by the electrodes plus the mean-field contribution from the other electron, are plotted as dashed lines.

$$h^A_{ij}=\sum_{\alpha=0}^{K^A}\sum_{\beta=0}^{K^A}B^{A*}_{\alpha i}B^A_{\beta j}h^A_{\alpha\beta}, \tag{D1}$$

$$u_{ij,kl} = \sum_{\alpha=0}^{K^L}\sum_{\beta=0}^{K^R} B^{L*}_{\alpha i} B^{R*}_{\beta j} B^{L}_{\alpha k} B^{R}_{\beta l} u^{LR}_{\alpha\beta}, \tag{D2}$$

where Greek letters denote matrix elements in the sinc-DVR basis, and Latin letters are for the Hartree basis.

Upon inserting the wave-function ansatz into the time-independent Schrödinger equation and projecting onto a two-body state $\left\langle \phi^L_i \phi^R_j \right|$, we get

$$\langle \phi^L_i \phi^R_j | \hat{H} | \Phi_n \rangle = \sum_{k=0}^{N^L}\sum_{l=0}^{N^R} H_{ij,kl} C_{kl,n} = C_{ij,n} E_n,$$

where the $H_{ij,kl} \equiv \langle \phi^L_i \phi^R_j | \hat{H} | \phi^L_k \phi^R_l \rangle$ are the matrix elements of the Hamiltonian in the Hartree product basis. The solution of this eigenvalue equation yields the coefficients $C_{ij,n}$, where each column corresponds to an eigenstate $|\Phi_n\rangle$ with corresponding eigenenergy E_n. The matrix elements of the two-body Hamiltonian can be expressed as

$$H_{ij,kl} = h^L_{ik}\delta_{jl} + \delta_{ik} h^R_{jl} + u_{ij,kl},$$

where the one- and two-body matrix elements in the Hartree basis are shown in Eqs. (D1) and (D2).

APPENDIX E: THE VON NEUMANN ENTROPY

The von Neumann entropy is defined by

$$S = -\mathrm{tr}[\hat{\rho} \log_2(\hat{\rho})],$$

where $\hat{\rho}$ is the density operator. The entropy of the eigenstates $|\Phi_n\rangle$ will be zero as they are pure states. However, the entropy of the reduced subsystems (L and R) of $|\Phi_n\rangle$ will in general not be zero. Each subsystem will have the same entropy, and any nonzero entropy can be attributed to entanglement. We can evaluate the entanglement entropy by bypassing the construction of the reduced density operator and using the Schmidt decomposition instead. Specifically, for a given two-body wave function $|\Psi\rangle$ expressed in terms of the Hartree product states,

$$|\Psi\rangle = \sum_{k=0}^{N^L}\sum_{l=0}^{N^R} C_{kl} \left| \phi^L_k \phi^R_l \right\rangle,$$

we can perform a singular value decomposition of the two-body coefficients, $C_{kl} = \sum_{p=0}^{\tilde{N}} U_{kp}\sigma_p V^*_{lp}$, to obtain

$$|\Psi\rangle = \sum_{p=0}^{\tilde{N}} \sigma_p \left| \psi^L_p \psi^R_p \right\rangle,$$

where

$$\left|\psi^L_p\right\rangle \equiv \sum_{k=0}^{N^L} U_{kp} \left|\phi^L_k\right\rangle, \qquad \left|\psi^R_p\right\rangle \equiv \sum_{l=0}^{N^R} V^*_{lp} \left|\phi^R_l\right\rangle$$

are the Schmidt states, $\tilde{N}$ is either N^L or N^R depending on the definition of the singular value decomposition, and the σ_p are the singular values with σ_p^2 representing the occupation of the single-particle states $\left|\psi^L_p\right\rangle$ and $\left|\psi^R_p\right\rangle$. Using the singular values, we can then compute the von Neumann entropy of $|\Psi\rangle$ as

$$S = -\sum_{p=0}^{\tilde{N}} \sigma_p^2 \log_2(\sigma_p^2).$$

APPENDIX F: PARTICLE DENSITIES

For state $|\Psi\rangle$ above, we can compute the particle density as

$$\begin{aligned}\rho(x) &= \int \mathrm{d}y\, |\Psi(x,y)|^2 + \int \mathrm{d}y\, |\Psi(y,x)|^2 \\ &= \sum_{i,j=0}^{N^L}\sum_{l=0}^{N^R} C^*_{il} C_{jl} \phi^{L*}_i(x)\phi^L_j(x) \\ &\quad + \sum_{i,j=0}^{N^R}\sum_{k=0}^{N^L} C^*_{ki} C_{kj} \phi^{R*}_i(x)\phi^R_j(x),\end{aligned}$$

which collapses to the electron density in the case of indistinguishable particles. The calculated particle densities for the three target configurations found through numerical optimization in this work are shown in Fig. 7.

APPENDIX G: FINDING OPTIMAL WELL CONFIGURATIONS

In this appendix, we present a way of finding the optimal configuration for single motional qubit rotations, configuration I, as well as the optimal configurations for two-qubit operations, configurations II and III. These are found by expressing our configurational search in terms of an optimization problem. The seven voltages of the potential from Eq. (1), denoted **V**, will be varied to find the optimal solution. We note that, due to the flexibility provided by the potential, the optimization landscape consists of several local minima and the resulting voltages are therefore somewhat arbitrary. The same can also be said for the path between configurations. We have chosen configurations and a path such that our results resemble those of Fig. 2(b) by Zhao *et al.* [88], but we stress that our model allows for vastly different solutions. We select a fixed anharmonicity with equal magnitude and opposite sign for each well, and

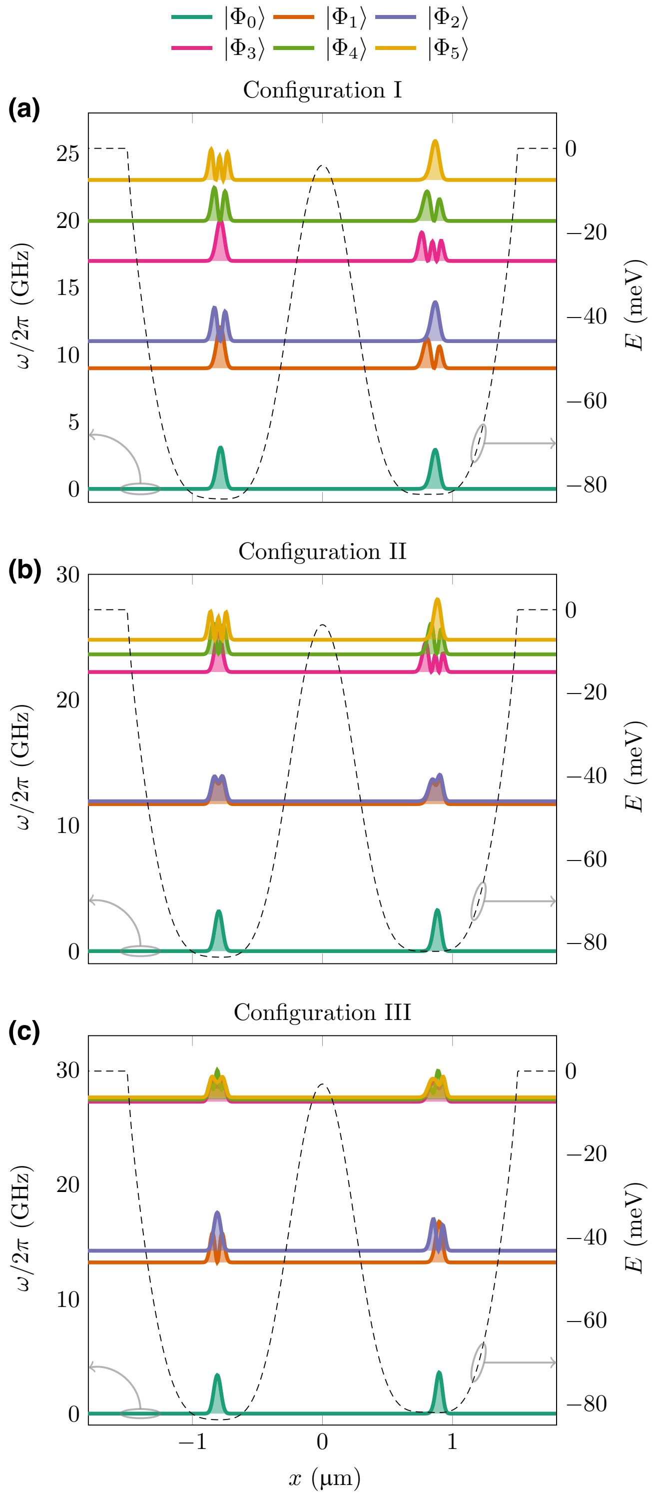

FIG. 7. Calculated particle densities of the first six eigenstates of the full two-body Hamiltonian for configurations I (a), II (b), and III (c). Each state is shifted upwards with its transition frequency from the ground state (in teal). The electrostatic potential wells are shown with dashed lines. Note that these are hybrid plots; the left y axis gives the unit scale for the transition frequencies, while the right y axis gives the unit scale for the electrostatic potential energy, as indicated by the arrows.

try to tune the wells such that only the detuning between each well is altered.

Configuration I is a configuration for which the transition frequencies are distinct, but at the same time within the working range of 5–15 GHz of the readout resonators. Furthermore, we aim for the anharmonicities in the left and right wells, denoted $\beta^L/2\pi$ and $\beta^R/2\pi$, to have equal magnitudes but opposite signs. This adjustment is made to eliminate *ZZ* crosstalk and facilitate a high on:off ratio for the implementation of controlled-phase gates [88,89]. There are several possible candidates for the transition frequencies and anharmonicities that satisfy these requirements, and the candidates we end up with are a result of performing the optimization process for a range of possible candidates. For the left well, we targeted a transition frequency between the two lowest-energy levels of $\omega^L/2\pi = \epsilon_1^L - \epsilon_0^L = 11\,\text{GHz}$, and a corresponding transition frequency for the right well of $\omega^R/2\pi = \epsilon_1^R - \epsilon_0^R = 9\,\text{GHz}$. Here the ϵ_i^A are the Hartree eigenvalues, i.e., the single-particle Hartree energies. At the same time, we targeted anharmonicities of $\beta^L/2\pi = -\beta^R/2\pi = 1\,\text{GHz}$. If we were allowed to vary the transition frequencies and anharmonicities independently and freely, a cost function with minima that coincide with these properties is

$$\begin{aligned} C_{\text{I}}(\mathbf{V}) = {} & [\omega^L(\mathbf{V})/2\pi - 11\,\text{GHz}]^2 \\ & + [\omega^R(\mathbf{V})/2\pi - 9\,\text{GHz}]^2 \\ & + [\beta^L(\mathbf{V})/2\pi - 1\,\text{GHz}]^2 \\ & + [\beta^R(\mathbf{V})/2\pi + 1\,\text{GHz}]^2, \end{aligned} \tag{G1}$$

where $\omega^A(\mathbf{V})/2\pi$ is the transition frequency and $\beta^A(\mathbf{V})/2\pi$ is the anharmonicity of the wells (with $A \in \{L, R\}$). To minimize $C_{\text{I}}(\mathbf{V})$, we evaluated its gradient with respect to the voltages, that is, $\nabla_{\mathbf{V}} C_{\text{I}}(\mathbf{V})$, using the Tensorflow machine learning library [94]. We then used a variation of the gradient descent method with an adaptive learning rate based on the ADAM algorithm [92], to update the voltages. The learning rate for the Adam optimizer was initially set to 10^{-4}.

For configuration III, we want to tune into a triple degeneracy point between states $|\Phi_3\rangle$, $|\Phi_4\rangle$, and $|\Phi_5\rangle$. This allows for the realization of a controlled-phase gate [89,90]. In such a configuration, we construct a cost function based on targeting the von Neumann entropies of the eigenstates $|\Phi_3\rangle$, $|\Phi_4\rangle$, and $|\Phi_5\rangle$ to be $S_3 = 1.5$, $S_4 = 1.0$, and $S_5 = 1.5$, respectively, while the entropies of the lower eigenstates should be kept minimal. We targeted the same anharmonicities as for configuration I, that is, $\beta^L/2\pi = -\beta^R/2\pi = 1\,\text{GHz}$. In order to end up with a configuration close to configuration I in parameter space, we utilized the parameters for configuration I, denoted $\mathbf{V}_{\text{I}}$, as the initial guess in the optimization algorithm. Finally, we ensure

TABLE I. Electrode voltages for configurations I, II, and III, resulting in a total electrostatic potential given by Eq. (1).

	I (mV)	II (mV)	III (mV)
V_1	297.45	296.41	295.17
V_2	152.33	155.01	158.23
V_3	344.36	342.63	340.56
V_4	−353.49	−354.66	−356.05
V_5	345.93	345.26	344.46
V_6	143.94	143.78	143.60
V_7	302.24	302.81	303.49

that a linear sweep of voltages from configuration I to configuration III passes through configuration II by targeting a detuning $\Delta_{\mathrm{III}}/2\pi = (\omega^L - \omega^R)/2\pi = -1$ GHz for configuration III, as explained in Sec. II F. The cost function we apply is given by

$$\begin{aligned} C_{\mathrm{III}}(\mathbf{V}) = {} & S_1(\mathbf{V})^2 \\ & + S_2(\mathbf{V})^2 \\ & + [S_3(\mathbf{V}) - 1.5]^2 \\ & + [S_4(\mathbf{V}) - 1.0]^2 \\ & + [S_5(\mathbf{V}) - 1.5]^2 \\ & + [\beta^L(\mathbf{V})/2\pi - 1\,\mathrm{GHz}]^2 \\ & + [\beta^R(\mathbf{V})/2\pi + 1\,\mathrm{GHz}]^2 \\ & + [\omega^L(\mathbf{V})/2\pi - \omega^R(\mathbf{V})/2\pi + 1\,\mathrm{GHz}]^2. \end{aligned} \tag{G2}$$

We used the same optimization method and learning rate as for configuration I.

APPENDIX H: OPTIMIZED ELECTRODE VOLTAGES

The explicit values of the electrode voltages obtained for the three optimized configurations are shown in Table I.

[1] M. Steffen, M. Ansmann, R. C. Bialczak, N. Katz, E. Lucero, R. McDermott, M. Neeley, E. M. Weig, A. N. Cleland, and J. M. Martinis, Measurement of the entanglement of two superconducting qubits via state tomography, Science **313**, 1423 (2006).

[2] R. Barends, *et al.*, Superconducting quantum circuits at the surface code threshold for fault tolerance, Nature **508**, 500 (2014).

[3] C. Monroe, D. M. Meekhof, B. E. King, W. M. Itano, and D. J. Wineland, Demonstration of a fundamental quantum logic gate, Phys. Rev. Lett. **75**, 4714 (1995).

[4] F. Schmidt-Kaler, H. Häffner, M. Riebe, S. Gulde, G. P. T. Lancaster, T. Deuschle, C. Becher, C. F. Roos, J. Eschner, and R. Blatt, Realization of the Cirac–Zoller controlled-NOT quantum gate, Nature **422**, 408 (2003).

[5] X. Li, Y. Wu, D. Steel, D. Gammon, T. H. Stievater, D. S. Katzer, D. Park, C. Piermarocchi, and L. J. Sham, An all-optical quantum gate in a semiconductor quantum dot, Science **301**, 809 (2003).

[6] J. R. Petta, A. C. Johnson, J. M. Taylor, E. A. Laird, A. Yacoby, H. D. Lukin, C. H. Marcus, H. P. Hanson, and A. C. Gossard, Coherent manipulation of coupled electron spins in semiconductor quantum dots, Science **309**, 2180+ (2005).

[7] B. W. Lovett, J. H. Reina, A. Nazir, and G. A. D. Briggs, Optical schemes for quantum computation in quantum dot molecules, Phys. Rev. B **68**, 205319 (2003).

[8] A. Nazir, B. W. Lovett, S. D. Barrett, J. H. Reina, and G. A. D. Briggs, Anticrossings in Förster coupled quantum dots, Phys. Rev. B **71**, 045334 (2005).

[9] M. V. G. Dutt, L. Childress, L. Jiang, E. Togan, J. Maze, F. Jelezko, A. S. Zibrov, P. R. Hemmer, and M. D. Lukin, Quantum register based on individual electronic and nuclear spin qubits in diamond, Science **316**, 1312 (2007).

[10] P. Neumann, R. Kolesov, B. Naydenov, J. Beck, F. Rempp, M. Steiner, V. Jacques, G. Balasubramanian, M. L. Markham, D. J. Twitchen, S. Pezzagna, J. Meijer, J. Twamley, F. Jelezko, and J. Wrachtrup, Quantum register based on coupled electron spins in a room-temperature solid, Nat. Phys. **6**, 249 (2010).

[11] H. Bernien, B. Hensen, W. Pfaff, G. Koolstra, M. S. Blok, L. Robledo, T. H. Taminiau, M. Markham, D. J. Twitchen, L. Childress, and R. Hanson, Heralded entanglement between solid-state qubits separated by three metres, Nature **497**, 86 (2013).

[12] I. S. Madjarov, J. P. Covey, A. L. Shaw, J. Choi, A. Kale, A. Cooper, H. Pichler, V. Schkolnik, J. R. Williams, and M. Endres, High-fidelity entanglement and detection of alkaline-earth Rydberg atoms, Nat. Phys. **16**, 857 (2020).

[13] S. J. Evered, D. Bluvstein, M. Kalinowski, S. Ebadi, T. Manovitz, H. Zhou, S. H. Li, A. A. Geim, T. T. Wang, N. Maskara, H. Levine, G. Semeghini, M. Greiner, V. Vuletic, and M. D. Lukin, High-fidelity parallel entangling gates on a neutral atom quantum computer, Nature **622**, 268 (2023).

[14] R. P. Feynman, Simulating physics with computers, Int. J. Theor. Phys. **21**, 467 (1982).

[15] A. Trabesinger, Quantum simulation, Nat. Phys. **8**, 263 (2012).

[16] I. M. Georgescu, S. Ashhab, and F. Nori, Quantum simulation, Rev. Mod. Phys. **86**, 153 (2014).

[17] E. Altman, *et al.*, Quantum simulators: Architectures and opportunities, PRX Quantum **2**, 017003 (2021).

[18] J. Carlson, D. J. Dean, M. Hjorth-Jensen, D. Kaplan, J. Preskill, K. Roche, M. J. Savage, and M. Troyer, Quantum computing for theoretical nuclear physics, a white paper prepared for the U.S. Department of Energy, Office of Science, Office of Nuclear Physics (2018).

[19] N. Klco and M. J. Savage, Systematically localizable operators for quantum simulations of quantum field theories, Phys. Rev. A **102**, 012619 (2020).

[20] A. Yamamoto and T. Doi, Toward nuclear physics from lattice QCD on quantum computers, PTEP **2024**, 033D02 (2024).

[21] M. Illa and M. J. Savage, Basic elements for simulations of standard-model physics with quantum annealers: Multigrid and clock states, Phys. Rev. A **106**, 052605 (2022).

[22] C. W. Bauer, *et al.*, Quantum simulation for high energy physics, PRX Quantum **4**, 027001 (2023).

[23] J. Smith, A. Lee, P. Richerme, B. Neyenhuis, P. W. Hess, P. Hauke, M. Heyl, D. A. Huse, and C. Monroe, Many-body localization in a quantum simulator with programmable random disorder, Nat. Phys. **12**, 907 (2016).

[24] W. Hofstetter and T. Qin, Quantum simulation of strongly correlated condensed matter systems, J. Phys. B: At., Mol. Opt. Phys. **51**, 082001 (2018).

[25] A. Smith, M. S. Kim, F. Pollmann, and J. Knolle, Simulating quantum many-body dynamics on a current digital quantum computer, npj Quantum Inf. **5**, 106 (2019).

[26] A. Peruzzo, J. McClean, P. Shadbolt, M.-H. Yung, X.-Q. Zhou, P. J. Love, A. Aspuru-Guzik, and J. L. O'Brien, A variational eigenvalue solver on a photonic quantum processor, Nat. Commun. **5**, 4213 (2014).

[27] M. Reiher, N. Wiebe, K. Svore, D. Wecker, and M. Troyer, Elucidating reaction mechanisms on quantum computers, Proc. Natl. Acad. Sci. **114**, 7555 (2016).

[28] A. Kandala, A. Mezzacapo, K. Temme, M. Takita, M. Brink, J. M. Chow, and J. M. Gambetta, Hardware-efficient variational quantum eigensolver for small molecules and quantum magnets, Nature **549**, 242 (2017).

[29] M. Greiner, O. Mandel, T. Esslinger, T. W. Hänsch, and I. Bloch, Quantum phase transition from a superfluid to a Mott insulator in a gas of ultracold atoms, Nature **415**, 39 (2002).

[30] R. A. Hart, P. M. Duarte, T.-L. Yang, X. Liu, T. Paiva, E. Khatami, R. T. Scalettar, N. Trivedi, D. A. Huse, and R. G. Hulet, Observation of antiferromagnetic correlations in the Hubbard model with ultracold atoms, Nature **519**, 211 (2015).

[31] S. Ebadi, T. T. Wang, H. Levine, A. Keesling, G. Semeghini, A. Omran, D. Bluvstein, R. Samajdar, H. Pichler, W. W. Ho, S. Choi, S. Sachdev, M. Greiner, V. Vuletić, and M. D. Lukin, Quantum phases of matter on a 256-atom programmable quantum simulator, Nature **595**, 227 (2021).

[32] B. Lanyon, C. Hempel, D. Nigg, M. Müller, R. Gerritsma, F. Zähringer, P. Schindler, J. Barreiro, M. Rambach, G. Kirchmair, M. Hennrich, P. Zoller, R. Blatt, and C. Roos, Universal digital quantum simulation with trapped ions, Science (New York, N.Y.) **334**, 57 (2011).

[33] C. Monroe, W. C. Campbell, L.-M. Duan, Z.-X. Gong, A. V. Gorshkov, P. W. Hess, R. Islam, K. Kim, N. M. Linke, G. Pagano, P. Richerme, C. Senko, and N. Y. Yao, Programmable quantum simulations of spin systems with trapped ions, Rev. Mod. Phys. **93**, 025001 (2021).

[34] A. Aspuru-Guzik and P. Walther, Photonic quantum simulators, Nat. Phys. **8**, 285 (2012).

[35] P. Alsing, *et al.*, Accelerating progress towards practical quantum advantage: The quantum technology demonstration project roadmap, ArXiv:2210.14757.

[36] C. Matthiesen, Q. Yu, J. Guo, A. M. Alonso, and H. Häffner, Trapping electrons in a room-temperature microwave Paul trap, Phys. Rev. X **11**, 011019 (2021).

[37] Q. Yu, A. M. Alonso, J. Caminiti, K. M. Beck, R. T. Sutherland, D. Leibfried, K. J. Rodriguez, M. Dhital, B. Hemmerling, and H. Häffner, Feasibility study of quantum computing using trapped electrons, Phys. Rev. A **105**, 022420 (2022).

[38] P. M. Platzman and M. I. Dykman, Quantum computing with electrons floating on liquid helium, Science **284**, 1967 (1999).

[39] K. Shirahama, S. Ito, H. Suto, and K. Kono, Surface study of liquid ^{3}He using surface state electrons, J. Low Temp. Phys. **101**, 439 (1995).

[40] M. Dykman, P. Platzman, and P. Seddighrad, Qubits with electrons on liquid helium, Phys. Rev. B **67**, 155402 (2003).

[41] A. J. Dahm, J. Heilman, I. Karakurt, and T. Peshek, Quantum computing with electrons on helium, Physica E **18**, 169 (2003).

[42] D. I. Schuster, A. Fragner, M. I. Dykman, S. A. Lyon, and R. J. Schoelkopf, Proposal for manipulating and detecting spin and orbital states of trapped electrons on helium using cavity quantum electrodynamics, Phys. Rev. Lett. **105**, 040503 (2010).

[43] X. Shi, L. Wei, and C. H. Oh, Quantum computation with surface-state electrons by rapid population passages, Sci. China Phys. Mech. Astron. **57**, 1718 (2014).

[44] E. Kawakami, J. Chen, M. Benito, and D. Konstantinov, Hybrid Rydberg-spin qubit of electrons on helium, Phys. Rev. Applied **20**, 054022 (2023).

[45] S. Lyon, Spin-based quantum computing using electrons on liquid helium, Phys. Rev. A **74**, 052338 (2006).

[46] M. Dykman, O. Asban, Q. Chen, D. Jin, and S. Lyon, Spin dynamics in quantum dots on liquid helium, Phys. Rev. B **107**, 035437 (2023).

[47] D. Marty, Stability of two-dimensional electrons on a fractionated helium surface, J. Phys. C: Solid State Phys. **19**, 6097 (1986).

[48] H. Ikegami, H. Akimoto, and K. Kono, Nonlinear transport of the Wigner solid on superfluid ^{4}He in a channel geometry, Phys. Rev. Lett. **102**, 046807 (2009).

[49] M. Zhang, H. Y. Jia, and L. F. Wei, Jaynes-Cummings models with trapped electrons on liquid helium, Phys. Rev. A **80**, 055801 (2009).

[50] D. G. Rees, N. R. Beysengulov, Y. Teranishi, C.-S. Tsao, S.-S. Yeh, S.-P. Chiu, Y.-H. Lin, D. A. Tayurskii, J.-J. Lin, and K. Kono, Structural order and melting of a quasi-one-dimensional electron system, Phys. Rev. B **94**, 045139 (2016).

[51] S. Zou and D. Konstantinov, Image-charge detection of the Rydberg transition of electrons on superfluid helium confined in a microchannel structure, New J. Phys. **24**, 103026 (2022).

[52] G. Papageorgiou, P. Glasson, K. Harrabi, V. Antonov, E. Collin, P. Fozooni, P. Frayne, M. Lea, Y. Mukharsky, and D. Rees, Counting individual trapped electrons on liquid helium, Appl. Phys. Lett. **86**, 153106 (2004).

[53] D. G. Rees, I. Kuroda, C. A. Marrache-Kikuchi, M. Höfer, P. Leiderer, and K. Kono, Point-contact transport properties of strongly correlated electrons on liquid helium, Phys. Rev. Lett. **106**, 026803 (2011).

[54] D. G. Rees, H. Totsuji, and K. Kono, Commensurability-dependent transport of a Wigner crystal in a nanoconstriction, Phys. Rev. Lett. **108**, 176801 (2012).

[55] G. Yang, A. Fragner, G. Koolstra, L. Ocola, D. A. Czaplewski, R. J. Schoelkopf, and D. I. Schuster, Coupling an ensemble of electrons on superfluid helium

to a superconducting circuit, Phys. Rev. X **6**, 011031 (2016).

[56] G. Koolstra, G. Yang, and D. I. Schuster, Coupling a single electron on superfluid helium to a superconducting resonator, Nat. Commun. **10**, 1 (2019).

[57] H. Byeon, K. Nasyedkin, J. R. Lane, N. R. Beysengulov, L. Zhang, R. Loloee, and J. Pollanen, Piezoacoustics for precision control of electrons floating on helium, Nat. Commun. **12**, 4150 (2021).

[58] E. Rousseau, Y. Mukharsky, D. Ponarine, O. Avenel, and E. Varoquaux, Trapping electrons in electrostatic traps over the surface of ^{4}He, J. Low Temp. Phys. **148**, 193 (2007).

[59] F. Bradbury, M. Takita, T. Gurrieri, K. Wilkel, K. Eng, M. Carroll, and S. Lyon, Efficient clocked electron transfer on superfluid helium, Phys. Rev. Lett. **107**, 266803 (2011).

[60] X. Zhou, G. Koolstra, X. Zhang, G. Yang, X. Han, B. Dizdar, X. Li, R. Divan, W. Guo, K. W. Murch, D. I. Schuster, and D. Jin, Single electrons on solid neon as a solid-state qubit platform, Nature **605**, 46 (2022).

[61] X. Zhou, X. Li, Q. Chen, G. Koolstra, G. Yang, B. Dizdar, Y. Huang, C. S. Wang, X. Han, X. Zhang, D. I. Schuster, and D. Jin, Electron charge qubit with 0.1 millisecond coherence time, Nat. Phys. **20**, 116 (2023).

[62] C. J. Cramer, *Essentials of Computational Chemistry* (Wiley, New York, 2004).

[63] A. Blais, A. L. Grimsmo, S. M. Girvin, and A. Wallraff, Circuit quantum electrodynamics, Rev. Mod. Phys. **93**, 025005 (2021).

[64] G. Burkard, T. D. Ladd, A. Pan, J. M. Nichol, and J. R. Petta, Semiconductor spin qubits, Rev. Mod. Phys. **95**, 025003 (2023).

[65] D. Loss and D. P. DiVincenzo, Quantum computation with quantum dots, Phys. Rev. A **57**, 120 (1998).

[66] G. Burkard, D. Loss, and D. P. DiVincenzo, Coupled quantum dots as quantum gates, Phys. Rev. B **59**, 2070 (1999).

[67] D. N. Pham, S. Bharadwaj, and L. Ram-Mohan, Spatial entanglement in two-dimensional artificial atoms, J. Appl. Phys. **135**, 064401 (2024).

[68] E. Nielsen, R. Rahman, and R. P. Muller, A many-electron tight binding method for the analysis of quantum dot systems, J. Appl. Phys. **112**, 114304 (2012).

[69] E. Nielsen, R. W. Young, R. P. Muller, and M. S. Carroll, Implications of simultaneous requirements for low-noise exchange gates in double quantum dots, Phys. Rev. B **82**, 075319 (2010).

[70] X. Hu and S. D. Sarma, Hilbert-space structure of a solid-state quantum computer: Two-electron states of a double-quantum-dot artificial molecule, Phys. Rev. A **61**, 062301 (2000).

[71] C. Barthel, D. Reilly, C. M. Marcus, M. Hanson, and A. Gossard, Rapid single-shot measurement of a singlet-triplet qubit, Phys. Rev. Lett. **103**, 160503 (2009).

[72] L. A. Orona, J. M. Nichol, S. P. Harvey, C. G. Bøttcher, S. Fallahi, G. C. Gardner, M. J. Manfra, and A. Yacoby, Readout of singlet-triplet qubits at large magnetic field gradients, Phys. Rev. B **98**, 125404 (2018).

[73] M. Reed, B. Maune, R. Andrews, M. Borselli, K. Eng, M. Jura, A. Kiselev, T. Ladd, S. Merkel, I. Milosavljevic, *et al.*, Reduced sensitivity to charge noise in semiconductor spin qubits via symmetric operation, Phys. Rev. Lett. **116**, 110402 (2016).

[74] Y. Monarkha and K. Kono, *Two-Dimensional Coulomb Liquids and Solids* (Springer Science & Business Media, Berlin, Germany, 2013), Vol. 142.

[75] M. W. Cole and M. H. Cohen, Image-potential-induced surface bands in insulators, Phys. Rev. Lett. **23**, 1238 (1969).

[76] V. Shikin, Some properties of surface electrons in liquid helium, Sov. Phys. JETP **33**, 387 (1971).

[77] C. C. Grimes, T. R. Brown, M. L. Burns, and C. L. Zipfel, Spectroscopy of electrons in image-potential-induced surface states outside liquid helium, Phys. Rev. B **13**, 140 (1976).

[78] E. Collin, W. Bailey, P. Fozooni, P. G. Frayne, P. Glasson, K. Harrabi, M. J. Lea, and G. Papageorgiou, Microwave saturation of the Rydberg states of electrons on helium, Phys. Rev. Lett. **89**, 245301 (2002).

[79] F. Wagner, Scattering of light by thermal ripplons on superfluid helium, J. Low Temp. Phys. **13**, 317 (1973).

[80] C. C. Grimes and G. Adams, Evidence for a liquid-to-crystal phase transition in a classical, two-dimensional sheet of electrons, Phys. Rev. Lett. **42**, 795 (1979).

[81] J. I. Cirac and P. Zoller, Quantum computations with cold trapped ions, Phys. Rev. Lett. **74**, 4091 (1995).

[82] S. Sheldon, E. Magesan, J. M. Chow, and J. M. Gambetta, Procedure for systematically tuning up crosstalk in the cross-resonance gate, Phys. Rev. A **93**, 060302 (2016).

[83] S. Kvaal, M. Hjorth-Jensen, and H. M. Nilsen, Effective interactions, large-scale diagonalization, and one-dimensional quantum dots, Phys. Rev. B **76**, 085421 (2007).

[84] This claim was validated by also doing full configuration-interaction calculations with fermionic antisymmetry between the electrons. All such calculations led to similar results as those we present here with distinguishable electrons.

[85] F. W. Strauch, P. R. Johnson, A. J. Dragt, C. J. Lobb, J. R. Anderson, and F. C. Wellstood, Quantum logic gates for coupled superconducting phase qubits, Phys. Rev. Lett. **91**, 167005 (2003).

[86] L. DiCarlo, J. M. Chow, J. M. Gambetta, L. S. Bishop, B. R. Johnson, D. Schuster, J. Majer, A. Blais, L. Frunzio, S. Girvin, *et al.*, Demonstration of two-qubit algorithms with a superconducting quantum processor, Nature **460**, 240 (2009).

[87] M. A. Nielsen and I. L. Chuang, *Quantum Computation and Quantum Information* (Cambridge University Press, Cambridge, 2010).

[88] P. Zhao, P. Xu, D. Lan, J. Chu, X. Tan, H. Yu, and Y. Yu, High-contrast *ZZ* interaction using superconducting qubits with opposite-sign anharmonicity, Phys. Rev. Lett. **125**, 200503 (2020).

[89] J. Ku, X. Xu, M. Brink, D. C. McKay, J. B. Hertzberg, M. H. Ansari, and B. L. T. Plourde, Suppression of unwanted *ZZ* interactions in a hybrid two-qubit system, Phys. Rev. Lett. **125**, 200504 (2020).

[90] L. Xie, J. Zhai, Z. Zhang, J. Allcock, S. Zhang, and Y.-C. Zheng, in *Proceedings of the 27th ACM International*

Conference on Architectural Support for Programming Languages and Operating Systems, ASPLOS '22 (Association for Computing Machinery, New York, NY, USA, 2022), p. 499.

[91] In our discussions we refer to the Hartree states as our idealization of the noninteracting system. This is not entirely correct since the Hartree states do include correlations from the Coulomb interaction.

[92] D. P. Kingma and J. Ba, Adam: A method for stochastic optimization, ArXiv:1412.6980.

[93] D. T. Colbert and W. H. Miller, A novel discrete variable representation for quantum mechanical reactive scattering via the *S*-matrix Kohn method, J. Chem. Phys. **96**, 1982 (1992).

[94] M. Abadi, *et al.*, TensorFlow: Large-scale machine learning on heterogeneous systems, software available from https://www.tensorflow.org/.